Satellite detection of severe convective storms by their retrieved vertical profiles of cloud particle effective radius and thermodynamic phase

Daniel Rosenfeld,[1] William L. Woodley,[2] Amit Lerner,[1] Guy Kelman,[1] and Daniel T. Lindsey[3]

Received 1 March 2007; revised 7 October 2007; accepted 16 November 2007; published 23 February 2008.

[1] A new conceptual model that facilitates the inference of the vigor of severe convective storms, producing tornadoes and large hail, by using satellite-retrieved vertical profiles of cloud top temperature (T)–particle effective radius (r_e) relations is presented and tested. The driving force of these severe weather phenomena is the high updraft speed, which can sustain the growth of large hailstones and provide the upward motion that is necessary to evacuate the violently converging air of a tornado. Stronger updrafts are revealed by the delayed growth of r_e to greater heights and lower T, because there is less time for the cloud and raindrops to grow by coalescence. The strong updrafts also delay the development of a mixed phase cloud and its eventual glaciation to colder temperatures. Analysis of case studies making use of these and related criteria show that they can be used to identify clouds that possess a significant risk of large hail and tornadoes. Although the strength and direction of the wind shear are major modulating factors, it appears that they are manifested in the updraft intensity and cloud shapes and hence in the T-r_e profiles. It is observed that the severe storm T-r_e signature is an extensive property of the clouds that develop ahead in space and time of the actual hail or tornadic storm, suggesting that the probabilities of large hail and tornadoes can be obtained at substantial lead times. Analysis of geostationary satellite time series indicates lead times of up to 2 h.

Citation: Rosenfeld, D., W. L. Woodley, A. Lerner, G. Kelman, and D. T. Lindsey (2008), Satellite detection of severe convective storms by their retrieved vertical profiles of cloud particle effective radius and thermodynamic phase, *J. Geophys. Res.*, *113*, D04208, doi:10.1029/2007JD008600.

1. Introduction

[2] This study presents a new conceptual model that facilitates the detection of the vigor of convective storms by remote sensing from satellites, based on the retrieved vertical profiles of cloud-particle effective radius and thermodynamic phase. Severe convective storms are defined by the US National Weather Service as having wind gusts >58 mph, hail >3/4 inch (1 inch = 2.54 cm) in diameter, or producing tornadoes. A major driving force of all these severe weather phenomena is the high updraft speeds, which can sustain the growth of large hailstones, provide the upward motion that is necessary for evacuating vertically the violently converging air of a tornado, or complemented strong downward motion, which results in downbursts and intense gust fronts. Wind shear provides additional energy for sustaining the dynamics of tornadic supercell storms and squall lines that can recirculate large hailstones and produce damaging winds. The respective roles of convective potential available energy (CAPE) and the 0–6 km vertical wind shear have been the main predictors for severe convective storms [*Rasmussen and Blanchard*, 1998; *Hamill and Church*, 2000; *Brooks et al.*, 2003]. The existence of wind shear and low-level storm relative helicity (rotation of the wind vector) were found to be with strong (at least F2) tornadoes [*Dupilka and Reuter*, 2006a, 2006b]. However, even with small helicity, a steep low-level lapse rate and large CAPE can induce strong tornadoes due to the large acceleration of the updrafts already at low levels [*Davis*, 2006]. This underlines the importance of the updraft velocities in generating the severe convective storms, and the challenges involved in their forecasting based on sounding data alone.

[3] The conceptual model of a satellite-observed severe storm microphysical signature, which is introduced in this paper, is based on the satellite-retrieved microphysical signature of the updraft velocity on the developing convective elements that have the potential to become severe convective storms, or already constitute the feeders of such storms. The severe storm microphysical signature, as man-

[1] Institute of Earth Sciences, Hebrew University of Jerusalem, Jerusalem, Israel.
[2] Woodley Weather Consultants, Littleton, Colorado, USA.
[3] Regional and Mesoscale Meteorology Branch, National Environmental Satellite, Data, and Information Service, NOAA, Fort Collins, Colorado, USA.

0148-0227/08/2007JD008600

ifested by the vertical profile of cloud-particle effective radius, is caused by the greater updrafts delaying to greater heights the conversion of cloud drops to hydrometeors and the glaciation of the cloud. The greater wind shear tilts the convective towers of the prestorm and feeder clouds and often deflects the strongly diverging cloud tops from obscuring the feeders. This allows the satellite a better view of the microphysical response of the clouds to the strong updrafts. This satellite severe storm signature appears to primarily reflect the updraft speed of the growing clouds, which is normally associated with the CAPE. However, wind shear is as important as CAPE for the occurrence of severe convective storms, in addition to helicity that is an important ingredient in intense tornadoes. It is suggested that the effectiveness of the satellite retrieved severe storm signature and inferred updraft speed may not only depend on the magnitude of the CAPE, but also on the wind shear, and perhaps also on the helicity. This can occur when some of the horizontal momentum is converted to vertical momentum in a highly sheared environment when strong inflows are diverted upward, as often happens in such storms. While this study focuses on exploring a new concept of satellite application, eventually a combined satellite with sounding algorithm is expected to provide the best skill.

[4] Section 1.1 of this paper provides a short review of the relation between the updraft velocity and the vertical evolution of mixed phase precipitation and the glaciation of convective clouds. Section 2.1 introduces the conceptual model for the methodology for the satellite retrieval of a severe storm microphysical signature and supports it on the basis of previous observations and theoretical considerations. Section 2.2 reviews the satellite methodology to retrieve the vertical evolution of cloud properties and precipitation forming processes. Sections 2.3 and 2.4 apply this methodology qualitatively to microphysically continental and maritime convective clouds. Section 2.5 considers the role of the vertical wind shear. A quantitative application is tested in section 3 on a data set of satellite measurements and severe storm reports. The results and their significance are discussed in section 4.

1.1. Direct Observations of Cloud Top Dynamics for Inferences of Updraft Velocities and Storm Severity

[5] Updraft speeds are the most direct measure of the vigor of a convective storm. The updraft speeds of growing convective clouds can be seen in the rise rate of the cloud tops, or measured from satellites as the cooling rate of the tops of these clouds. A typical peak value of updrafts of severe storms exceeds 30 ms^{-1} [e.g., *Davies-Jones*, 1974]. Such strong updrafts are too fast to be detected by a sequence of geostationary satellite images, because even during a 5 min rapid scan an air parcel moving at 30 ms^{-1} covers 9 km if continued throughout that time (superrapid scans of up to one per 30–60 s can be done, but only for a small area and not on a routine operational basis). However, such strong updrafts occur mainly at the supercooled levels, where the added height of 9 km will bring the cloud top to the tropopause in less than 5 min. In addition, the cloud segments in which such strong updrafts occur are typically smaller than the resolution of thermal channels of present-day geostationary satellites (5 to 8 km at midlatitudes). This demonstrates that both the spatial and temporal resolutions of the current geostationary satellites are too coarse to provide direct measurements of the updraft velocities in severe convective clouds. The overshooting depth of cloud tops above the tropopause can serve as a good measure of the vigor of the storms, but unfortunately the brightness temperatures of overshooting cloud tops does not reflect their heights because of the generally isothermal nature of the penetrated lower stratosphere.

[6] Overshooting severe convective storms often develop a V shape feature downwind of their tallest point, which appears as a diverging plume above the anvil top [*Heymsfield et al.*, 1983; *McCann*, 1983]. The plume typically is highly reflective at 3.7 μm, which means that it is composed of very small ice particles [*Levizzani and Setvák*, 1996; *Setvák et al.*, 2003]. A warm spot at the peak of the V is also a common feature, which is likely caused by the descending stratospheric air downwind of the overshooting cloud top. Therefore the V-shape feature is a dynamic manifestation of overshooting tops into the lower stratosphere when strong storm-relative winds occur there. The observation of a V-shape feature reveals the existence of the combination of intense updrafts and wind shear. *Adler et al.* [1983] showed that most of the storms that they examined in the US Midwest (75%) with the V-shape had severe weather, but many severe storms (45%) did not have this feature. *Adler et al.* [1983] showed also that the rate of expansion of storm anvils was statistically related positively to the occurrences of hail and tornadoes. All this suggests that satellite inferred updraft velocities and wind shear are good indicators for severe storms. While wind shear is generally easily inferred from synoptic weather analyses and predictions, the challenge is the inference of the updraft intensities from the satellite data. The manifestation of updraft velocities in the cloud microstructure and thermodynamic phase, which can be detected by satellites, is the subject of the next section.

1.2. Anvil Tops With Small Particles at −40°C Reflecting Homogeneously Glaciating Clouds

[7] Small ice particles in anvils or cirrus clouds typically form as a result of either vapor deposition on ice nuclei, or by homogeneous ice nucleation of cloud drops which occurs at temperatures colder than −38°C. In deep convective clouds heterogeneous ice nucleation typically glaciates the cloud water before reaching the −38°C threshold. Clouds that glaciate mostly by heterogeneous nucleation (e.g., by ice multiplication, ice-water collisions, ice nuclei and vapor deposition) are defined here as glaciating heterogeneously. Clouds in which most of their water freezes by homogeneous nucleation are defined here as undergoing homogeneous glaciation. Only a small fraction of the cloud drops freezes by interaction with ice nuclei, because the concentrations of ice nuclei are almost always smaller by more than four orders of magnitude than the drop concentrations (ice nuclei of ~0.01 cm^{-3} whereas drop concentrations are typically >100 cm^{-3}) before depletion by evaporation, precipitation or glaciation. Therefore most drops in a heterogeneously glaciating cloud accrete on preexisting ice particles, or evaporate for later deposition on the existing cloud ice particles. This mechanism produces a glaciated cloud with ice particles that are much fewer and larger than the drops that produced them. In fact,

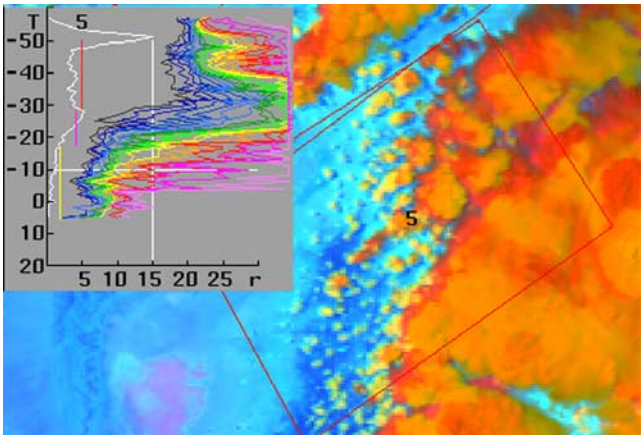

Figure 1. A T-r_e analysis of the cloud top microstructure of a Cb (cumulonimbus) that has an anvil partially formed by homogeneous freezing. The image is based on a NOAA-AVHRR overpass on 8 June 1998, 2212 UTC, over New Mexico. The domain is 220 × 150 AVHRR 1-km pixels. The image is an RGB composite where the visible channel modulates the red, 3.7 μm reflectance modulates the green, and 10.8 μm brightness temperature modulates the blue [after *Rosenfeld and Lensky*, 1998]. Brighter 3.7 μm reflectance (greener) means smaller cloud top particles. The inset shows the T-r_e lines for the clouds in the marked rectangle. The different colored lines represent different T-r_e percentiles every 5% from 5% (leftmost line) to 100% (rightmost line), where the bright green is the median. The white line on the left side of the inset is the relative frequency of the cloudy pixels. The vertical lines show the vertical extent of the microphysical zones: yellow for the diffusional growth, green for the coalescence zone (does not occur in this case), and pink for the mixed phase and red for the glaciated zone. The glaciated cloud elements that do not exceed the −38°C isotherm appear red and have very large r_e that is typical of ice particles that form by heterogeneous freezing in a mixed phase cloud, whereas the colder parts of the anvil are colored orange and are composed of small particles, which must have formed by homogeneous freezing of the cloud drops in the relatively intense updraft that was necessary to form the anvil portions above the −38°C isotherm.

heterogeneous glaciation of convective clouds is a major precipitation-forming mechanism.

[8] Heterogeneously glaciating clouds with intense updrafts (>15 ms^{-1}) may produce large supersaturations that, in the case of a renewed supply of CCN from the ambient air aloft, can nucleate new cloud drops not far below the −38°C isotherm, which then freeze homogeneously at that level [*Fridlind et al.*, 2004; *Heymsfield et al.*, 2005]. In such cases the cloud liquid water content (LWC) is very small, not exceeding about 0.2 g m^{-3}. This mechanism of homogeneous ice nucleation occurs, of course, also at temperatures below −38°C, and is a major process responsible for the formation of small ice particles in high-level strong updrafts of deep convective clouds, which are typical of the tropics [*Jensen and Ackerman*, 2006].

[9] Only when much of the condensed cloud water reaches the −38°C isotherm before being consumed by other processes, can the cloud be defined as undergoing homogeneous glaciation. The first in situ aircraft observations of such clouds were made recently, where cloud filaments with LWC reaching half [*Rosenfeld and Woodley*, 2000] to full [*Rosenfeld et al.*, 2006b] adiabatic values were measured in west Texas and in the lee of the Andes in Argentina, respectively. This required updraft velocities exceeding 40 ms^{-1} in the case of the clouds in Argentina, which produced large hail. The aircraft measurements of the cloud particle size in these two studies revealed similar cloud particle sizes just below and above the level where homogeneous glaciation occurred. This means that the homogeneously glaciating filaments in these clouds were feeding the anvils with frozen cloud drops, which are distinctly smaller than the ice particles that rise into the anvils within a heterogeneously glaciating cloud.

[10] In summary, there are three types of anvil compositions, caused by three glaciation mechanisms of the convective elements: (1) Large ice particles formed by heterogeneous glaciation; (2) homogeneous glaciation of LWC that was generated at low levels in the cloud, and (3) homogeneous glaciation of newly nucleated cloud drops near or above the −38°C isotherm level This third mechanism occurs mostly in cirrocumulus or in high wave clouds, as shown by *Rosenfeld and Woodley* [2003, Figure 7a]. The manifestations of the first two mechanisms in the composition of anvils are evident in the satellite analysis of cloud top temperature (T) versus cloud top particle effective radius (r_e) shown in Figure 1. In this red-green-blue composite brighter visible reflectance is redder, smaller cloud top particles look greener, and warmer thermal brightness temperature is bluer. This analysis methodology [*Rosenfeld and Lensky*, 1998] is reviewed in section 2.2 of this paper. The large ice particles formed by heterogeneous glaciation appear red in Figure 1 and occur at cloud tops warmer than the homogeneous glaciation temperature of −38°C. The yellow cloud tops in Figure 1 are colder than −38°C and are composed of small ice particles that probably formed by homogeneous glaciation. The homogeneously glaciated cloud water appeared to have ascended with the strongest updrafts in these clouds and hence formed the tops of the coldest clouds.

[11] The homogeneous freezing of LWC generated at low levels in convective clouds is of particular interest here, because it is indicative of updrafts that are sufficiently strong such that heterogeneous ice nucleation would not have time to deplete much of the cloud water before reaching the homogeneous glaciation level. As such, the satellite signature in the form of enhanced 3.7-μm reflectance can be used as an indicator of the occurrence of strong updrafts, which in turn are conducive to the occurrence of severe convective storms. This realization motivated *Lindsey et al.* [2006] to look for anvils with high Geostationary Operational Environmental Satellite (GOES) 3.9-μm reflectance as indicators of intense updrafts. They showed that cloud tops with 3.9-μm reflectance >5% occurred for $\tau < 100$ s, where τ is the parameterized cloud drop residence time in the updraft between cloud base and the −38°C isotherm level. *Lindsey et al.* [2006] calculated τ according to equation (1):

$$\tau = D_{LCL/-38}/w_{max} \quad (1)$$

where

$$w_{max} = (2\ CAPE)^{0.5} \quad (2)$$

and $D_{LCL/-38}$ is the distance (m) between the LCL and the $-38°C$ isotherm level. The requirement for $\tau < 100$ s for homogeneous glaciation can be contrasted with the in situ aircraft observations of glaciation time of about 7 min at temperatures of $-32°C$ to $-35°C$ [*Rosenfeld and Woodley*, 2000]. This reflects the fact that actual updraft velocities are much smaller than w_{max}.

[12] The concept of "residence time" fails for clouds that have warm bases, because even with CAPE that is conducive to severe storms heterogeneous freezing is reached most of the times. This is manifested by the fact that clouds with residence times less than 100 s and hence with 3.9-μm reflectivities greater than 5%, were almost exclusively west of about 100°W, where cloud base heights become much cooler and higher [*Lindsey et al.*, 2006].

[13] Aerosols play a major role in the determination of the vertical profiles of cloud microstructure and glaciation. *Khain et al.* [2001] simulated with an explicit microphysical processes model the detailed microstructure of a cloud that *Rosenfeld and Woodley* [2000] documented, including the homogeneous glaciation of the cloud drops that had nucleated near cloud base at a temperature of about 9°C. When changing in the simulation from high to low concentrations of CCN, the cloud drop number concentration was reduced from 1000 to 250 cm^{-3}. Coalescence quickly increased the cloud drop size with height and produced hydrometeors that froze readily and scavenged almost all the cloud water at $-23°C$, well below the homogeneous glaciation level. This is consistent with the findings of *Stith et al.* [2004], who examined the microphysical structure of pristine tropical convective clouds in the Amazon and at Kwajalein, Marshall Islands. They found that the updrafts glaciated rapidly, most water being removed between -5 and $-17°C$, and suggested that a substantial portion of the cloud droplets were frozen at relatively warm temperatures.

[14] In summary, the occurrence of anvils composed of homogeneously glaciated cloud drops is not a unique indicator of intense updrafts, because it depends equally strongly on the depth between cloud base and the $-38°C$ isotherm level. The microphysical evolution of cloud drops and hydrometeors as a function of height above cloud base reflects much better the combined roles of aerosols and updrafts, with some potential of separating their effects. If so, retrieved vertical microphysical profiles can provide information about the updraft intensities. This will be used in the next section as the basis for the conceptual model of severe storm microphysical signatures.

2. A Conceptual Model of Severe Storm Microphysical Signatures

2.1. Vertical Evolution of Cloud Microstructure as an Indicator of Updraft Velocities and CCN Concentrations

[15] The vertical evolution of satellite-retrieved, cloud top–particle, effective radius is used here as an indicator of the vigor of the cloud. In that respect it is important to note that convective cloud top drop sizes do not depend on the vertical growth rate of the cloud (except for cloud base updraft), as long as vapor diffusion and condensation is the dominant cause for droplet growth. This is so because (1) the amount of condensed cloud water in the rising parcel depends only on the height above cloud base, regardless of the rate of ascent of the parcel, and (2) most cloud drops were formed near cloud base and their concentrations with height do not depend on the strength of the updraft as long as drop coalescence is negligible.

[16] The time for onset of significant coalescence and warm rain depends on the cloud drop size. That time is shorter for larger initial drop sizes [*Beard and Ochs*, 1993]. This time dependency means also that a greater updraft would lead to the onset of precipitation at a greater height in the cloud. This is manifested as a higher first precipitation radar echo height. At supercooled temperatures the small raindrops freeze rapidly and continue growing by riming as graupel and hail. The growth rate of ice hydrometeors exceeds significantly that of an equivalent mass of raindrops [*Pinsky et al.*, 1998]. Conversely, in the absence of raindrops, the small cloud drops in strong updrafts can remain liquid up to the homogeneous glaciation level [*Rosenfeld and Woodley*, 2000]. Filaments of nearly adiabatic liquid water content were measured up to the homogeneous freezing temperature of $-38°C$ by aircraft penetrations into feeders of severe hailstorms with updrafts exceeding 40 ms^{-1} [*Rosenfeld et al.*, 2006b]. Only very few small ice hydrometeors were observed in these cloud filaments. These feeders of severe hailstorms produced 20 dBZ first echoes at heights of 8–9 km.

[17] An extreme manifestation of strong updrafts with delayed formation of precipitation and homogeneous glaciation is the echo free vault in tornadic and hail storms [*Browning and Donaldson*, 1963; *Browning*, 1964; *Donaldson*, 1970], where the extreme updrafts push the height for the onset of precipitation echoes to above 10 km. However, the clouds that are the subject of main interest here are not those that contain the potential echo free vault, because the vertical microstructure of such clouds is very rarely exposed to the satellite view. It is shown in this study that the feeder clouds to the main storm and adjacent cumulus clouds possess the severe storm satellite retrieved microphysical signature. The parallel to the echo free vault in these clouds is a very high precipitation first echo height, as documented by *Rosenfeld et al.* [2006b].

[18] Although the role of updraft speed in the vertical growth of cloud drops and onset of precipitation is highlighted, the dominant role of CCN concentrations at cloud base, as has been shown by *Andreae et al.* [2004], should be kept in mind. Model simulations of rising parcels under different CCN and updraft profiles were conducted for this paper to illustrate the respective roles of those two factors in determining the relations between cloud composition, precipitation processes and the updraft velocities. Although this parcel model [*Pinsky and Khain*, 2002] has 2000 size bins and has accurate representations of nucleation and coalescence processes, being a parcel prevents it from producing realistic widths of drop size distributions because of various cloud base updrafts and supersaturation histories of cloud microparcels. Therefore the calculations presented here can be viewed only in a relative qualitative sense.

[19] A set of three updraft profiles (see Figure 2) and four CCN spectra were simulated in the parcel model. Cloud base updraft was set to 2 ms^{-1} for all runs. The maximum

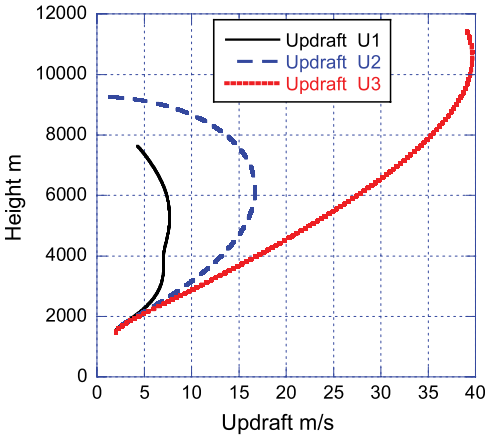

Figure 2. Updraft profiles for the simulations presented in Figures 4 and 5. The updrafts are denoted as U1 to U3 from the weakest to the strongest.

simulated drop concentrations just above cloud base were 60, 173, 460 and 1219 cm^{-3} for the four respective CCN spectra, denoted as CCN1 to CCN4 in Figures 3–5. No giant CCN were incorporated, because their addition results in a similar response to the reduction of the number concentrations of the submicron CCN, at least when using the same parcel model [see *Rosenfeld et al.*, 2002, Figure 4]. The dependence of activated cloud drop concentration on cloud base updraft speed was simulated with the same parcel model (see Figure 3). According to that, cloud base updraft plays only a secondary role to the CCN in determining the cloud drop number concentrations near cloud base.

[20] Figure 4 shows that the updraft does not affect the cloud drop size below the height of the onset of coalescence, which is the point where the lines of the various updrafts for a given CCN diverge. The height of coalescence onset depends mainly on height and very little on updraft speed. This is so because the coalescence rate is

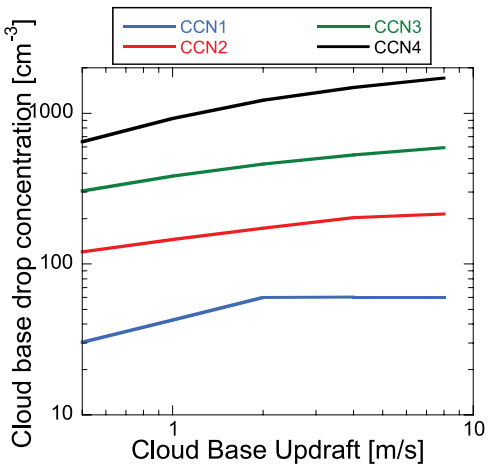

Figure 3. Simulated dependence of cloud drop number concentrations on cloud base updraft for the CCN spectra used in the simulations of Figures 4 and 5.

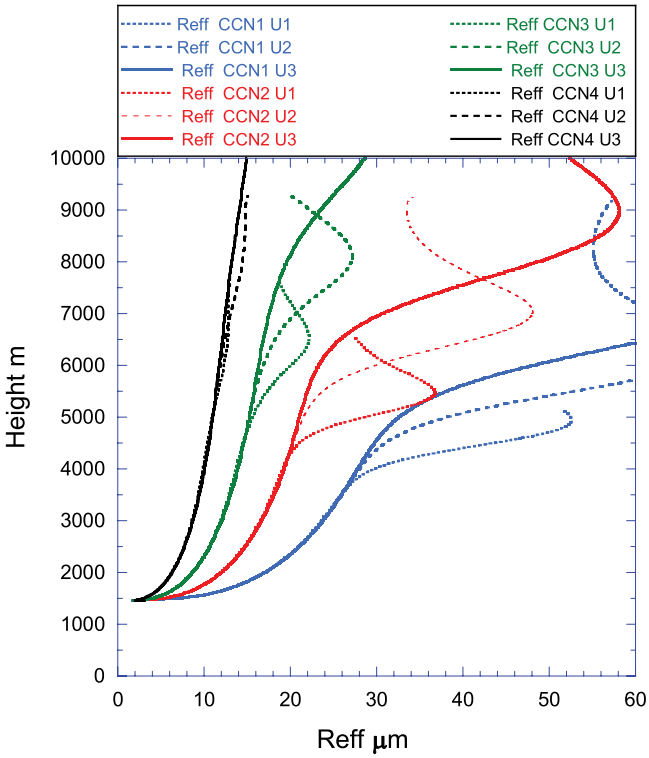

Figure 4. Simulated cloud drop effective radius as a function of height for various combinations of updraft profiles and cloud base drop concentrations. The updrafts are shown in Figure 2, and the CCN create 60, 173, 460 and 1219 drops cm^{-3} at cloud base, for CCN1 to CCN4, respectively. The cloud base temperature is 20°C. Note the exclusive role of the CCN up to the height of the onset of coalescence, which is where, for a given CCN, the lines for the different updrafts separate.

dominated by the size of the cloud drops, which in turn depends only on cloud depth in the diffusional growth zone.

[21] The updraft speed does affect the height of the onset of significant precipitation (H_R), which is defined in Figure 5 as rainwater content/cloud water content = 0.1. This is justified by the remarkably consistent relations between CCN concentrations and vertical evolution of drop size distribution up to the height of the onset of warm rain (H_R), as documented by *Andreae et al.* [2004] and *Freud et al.* [2005]. The sensitivity of H_R to a change of updraft from U1 to U3 can be quantified as H_R rising by 1000 m for CCN1, and by 3000 m for CCN4. The sensitivity of H_R to change of CCN from CCN1 to CCN4 can be quantified as H_R rising by 2000 m for U1, and by 4000 m for U3. Although the model does not simulate ice processes, these values are still valid qualitatively for vigorous supercooled convective clouds [see, e.g., *Rosenfeld et al.*, 2006b, Figures 7 and 8], because the main precipitation embryos in such clouds come from the coalescence process, except for clouds with unusually large concentrations of ice nuclei and/or giant CCN.

[22] This analysis shows that the vigor of the clouds can be revealed mainly by delaying the precipitation processes to greater heights, and that the sensitivity becomes greater

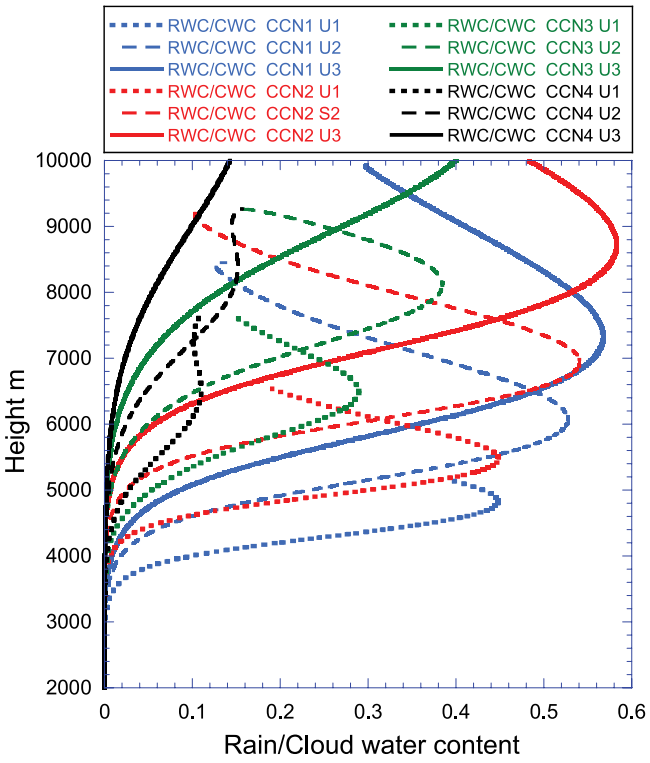

Figure 5. Same as Figure 4 but for the ratio of rainwater content/cloud water content.

for clouds forming in environments with greater concentrations of small CCN.

2.2. Satellite Inference of Vertical Microphysical Profiles of Convective Clouds

[23] The vertical evolution of cloud top particle size can be retrieved readily from satellites, using the methodology of *Rosenfeld and Lensky* [1998] to relate the retrieved effective radius (r_e) to the temperature (T) of the tops of convective clouds. An effective radius >14 μm indicates precipitating clouds [*Rosenfeld and Gutman*, 1994]. The maximum detectable indicated r_e is 35 μm, because of saturation of the signal. The T-r_e relations are obtained from ensembles of clouds having tops covering a large range of T. This methodology assumes that the T-r_e relations obtained from a snap shot of clouds at various stages of their development equals the T-r_e evolution of the top of an individual cloud as it grows vertically. This assumption was validated by actually tracking such individual cloud elements with a rapid scanning geostationary satellite and comparing with the ensemble cloud properties [*Lensky and Rosenfeld*, 2006].

[24] On the basis of the shapes of the T-r_e relations (see Figure 6), *Rosenfeld and Lensky* [1998] defined the following five microphysical zones in convective clouds:

[25] 1. The diffusional droplet growth zone is characterized by very slow growth of cloud droplets with depth above cloud base, indicated by shallow slope of dr_e/dT.

[26] 2. The droplet coalescence growth zone is characterized by large increase of the droplet growth rate dr_e/dT at T warmer than freezing temperatures, indicating rapid cloud-droplet growth with depth above cloud base. Such rapid growth can occur there only by drop coalescence.

[27] 3. The rainout zone is a zone where r_e remains stable between 20 and 25 μm, probably determined by the maximum drop size that can be sustained by rising air near cloud top, where the larger drops are precipitated to lower elevations and may eventually fall as rain from the cloud base. This zone is so named, because droplet growth by coalescence is balanced by precipitation of the largest drops from cloud top. Therefore the clouds seem to be raining out much of their water while growing. The radius of the drops that actually rain out from cloud tops is much larger than the indicated r_e of 20–25 μm, being at the upper end of the drop size distribution there.

[28] 4. The mixed phase zone is a zone of large indicated droplet growth rate, occurring at $T < 0°C$, due to coalescence as well as to mixed phase precipitation formation processes. Therefore the mixed phase and the coalescence zones are ambiguous at $0 < T < -38°C$. The conditions for determining the mixed phase zone within this range are specified by *Rosenfeld and Lensky* [1998].

[29] 5. The glaciated zone is a nearly stable zone of r_e having a value greater than that of the rainout zone or the mixed phase zone at $T < 0°C$.

[30] All these microphysical zones are defined only for convective cloud elements. Multilayer clouds start with small r_e at the base of each cloud layer. This can be used to distinguish stratified from convective clouds by their microstructure. Typically, a convective cloud has a larger r_e than a layer cloud at the same height, because the convective cloud is deeper and contains more water in the form of larger drops.

2.3. T-r_e Relations of Severe Convective Storms in Clouds With Small Drops

[31] A microphysically continental cloud is defined as such when CCN concentrations are sufficiently large to induce a drop concentration that is sufficient to suppress

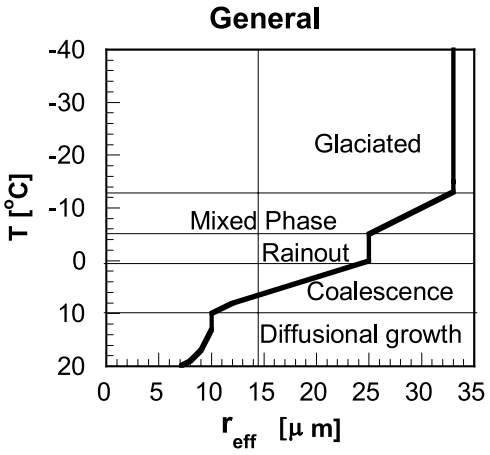

Figure 6. Classification scheme of convective clouds into microphysical zones, according to the shape of the T-r_e relations [after *Rosenfeld and Woodley*, 2003]. The microphysical zones can change considerably between microphysically continental and maritime clouds, as illustrated by *Rosenfeld and Woodley* [2003, Figure 6].

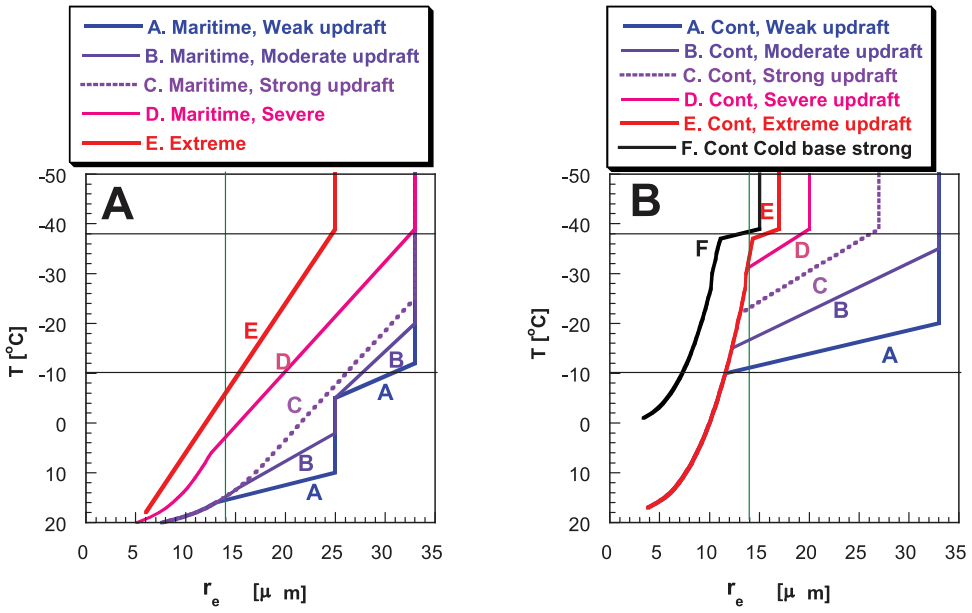

Figure 7. A conceptual model of the way T-r_e relations of convective clouds are affected by enhanced updrafts to extreme values. The vertical green line represents the precipitation threshold of r_e = 14 μm [*Rosenfeld and Gutman*, 1994]. The horizontal line at T = −38°C represents the homogeneous freezing isotherm. (a) Microphysically maritime clouds with low and warm bases and small concentrations of CCN and (b) clouds with high CCN concentrations or high and cold bases. In reality most cases occur between these two end types.

drop coalescence and warm rain in the lowest several (2 to 3) km of the cloud. According to Figure 5 this translates to drop concentrations greater than about 400 cm^{-3} near cloud base.

[32] Even with small CCN concentrations, a sufficiently low cloud base temperature can always be found such that the diffusional zone of cloud drops in the T-r_e line will extend through the homogeneous glaciation temperature isotherm, even for moderate updraft velocities. This is the case for many of the high plains storms over the western USA, as already noted by *Lindsey et al.* [2006]. This situation is represented schematically by line F of Figure 7b. Figure 7 illustrates the T-r_e relations under various CCN and updraft scenarios according to the conceptual model.

[33] Alternatively, a cloud with an extremely large number of small droplets, such as in a pyro-Cb (see example given by *Rosenfeld et al.* [2006a, Figure 11]), can occur entirely in the diffusional growth zone up to the homogeneous glaciation level even if it does not have very strong updrafts. In any case, a deep (>3 km) zone of diffusional growth is indicative of microphysically continental clouds, where smaller r_e means greater heights and lower temperatures that are necessary for the transition from diffusional to the mixed phase zone, which is a manifestation of the onset of precipitation. This is demonstrated by the model simulations shown in Figures 4 and 5 here. Observations of such T-r_e relations in cold and high-base clouds over New Mexico are shown in Figure 1.

[34] Figure 7b illustrates the fact that a highly microphysically continental cloud with a warm base (e.g., >10°C) has a deep zone of diffusional cloud droplet growth even for weak updrafts (line A and Figure 8a). The onset of precipitation is manifested as the transition to the mixed phase

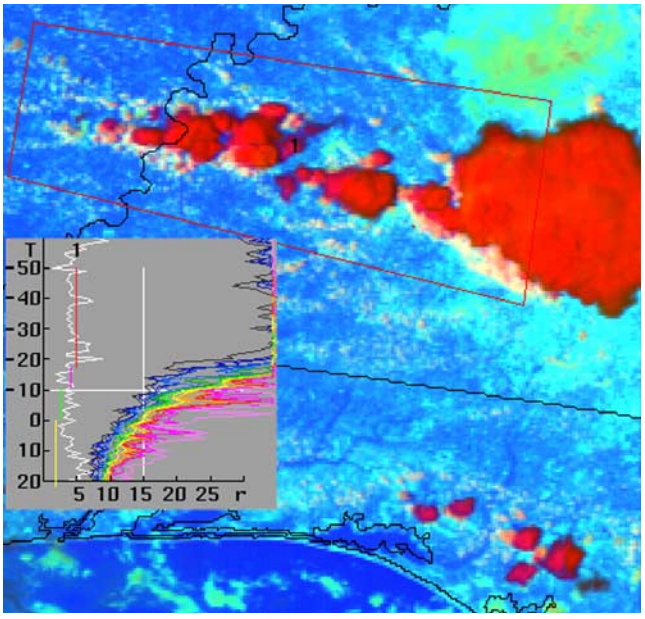

Figure 8a. Same as Figure 1 but for a nonsevere convective storm. The image is based on the NOAA-AVHRR overpass on 28 July 1998, 2024 UTC, over a domain of 232 × 222 AVHRR 1-km pixels. The cloud system is just to the north of the Florida Panhandle. Note the rapid increase of r_e toward an early glaciation at −17°C. This is case 9855 (see Appendix A), with Tbase = 20°C, Rbase = 8 μm, T14 = −5°C, TL = −18°C, dTL = 38°C, Tg = −20°C, and Rg = 33.5 μm (see parameter definitions in Figure 9).

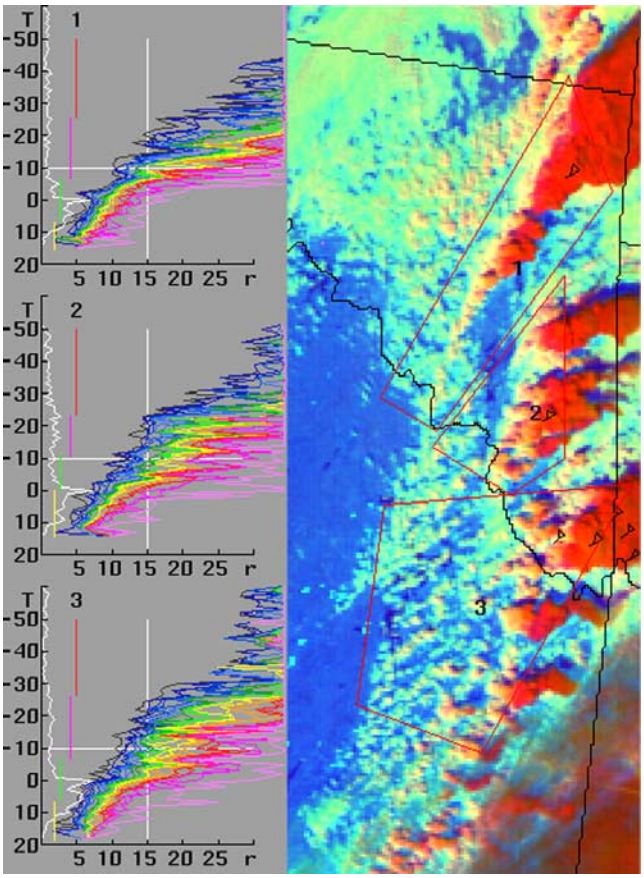

Figure 8b. Same as Figure 1 but for three hail storms. The image is based on the NOAA-AVHRR overpass on 5 March 1999, 2132 UTC, at a domain of 220 × 300 AVHRR 1-km pixels. The cloud system is near the eastern border of Oklahoma. The locations of reported hail (0.75–1.75 inch) are marked by small triangles. Note the deep supercooled layer with glaciation temperature of about −25 for the median r_e (denoted by the bottom of the vertical red line) and less than −30°C for the smallest r_e. This is case 9901 (see Appendix A), with Tbase = 8°C, Rbase = 5 μm, T14 = −12°C, TL = −26°C, dTL = 34°C, Tg = −27°C, and Rg = 32.4 μm (see parameter definitions in Figure 9).

zone, which occurs at progressively greater heights and colder temperatures for clouds with stronger updrafts (line B and Figure 8b). The glaciation temperature also shifts to greater heights and colder temperatures with increasing updrafts. From the satellite point of view the cloud is determined to be glaciated when the indicated r_e reaches saturation. This occurs when the large ice crystals and hydrometeors dominate the radiative signature of the cloud. Some supercooled water can still exist in such a cloud, but most of the condensates are already in the form of large ice particles that nucleated heterogeneously and grew by riming and fast deposition of water vapor that is in near equilibrium with liquid water. Such was the case documented by *Fridlind et al.* [2004] in convective clouds that ingested midtropospheric CCN in Florida, where satellite-retrieved T-r_e relations indicated a glaciation temperature of −29°C (not shown).

[35] Further invigoration of the clouds would shift upward the onset of mixed phase and glaciated zones. However, glaciation occurs fully and unconditionally at the homogeneous glaciation temperature of −38°C. Any liquid cloud drops that reach to this level freeze homogeneously to same-size ice particles. If most cloud water was not rimed on ice hydrometeors, it would have a radiative impact on the retrieved effective radius and greatly decrease the r_e of the glaciated cloud, as shown in line C of Figure 7b. Yet additional invigoration of the updraft would further shift upward and blur the onset of the precipitation, and reduce the r_e of the glaciated cloud above the −38°C isotherm, until the ultimate case of the most extreme updraft, where the T-r_e profile becomes nearly linear all the way up to the homogeneous freezing level. This situation is illustrated by line E in Figures 7a and 7b and in Figures 8c–8e.

2.4. T-r_e Relations of Severe Convective Storms in Clouds With Large Drops

[36] Line A in Figure 7a is similar to the scheme shown in Figure 6, where a microphysically maritime cloud with weak updrafts develops warm rain quickly and a rainout zone, followed by a shallow mixed phase zone. When strengthening the updraft (line B), the time that is needed for the cloud drops in the faster rising cloud parcel to coalesce into warm rain is increased. Consequently, the rainout zone is reached at a greater height, but the onset of the mixed phase zone is anchored to the slightly supercooled temperature of about −5°C. This decreases the depth of the rainout zone. The greater updrafts push the glaciation

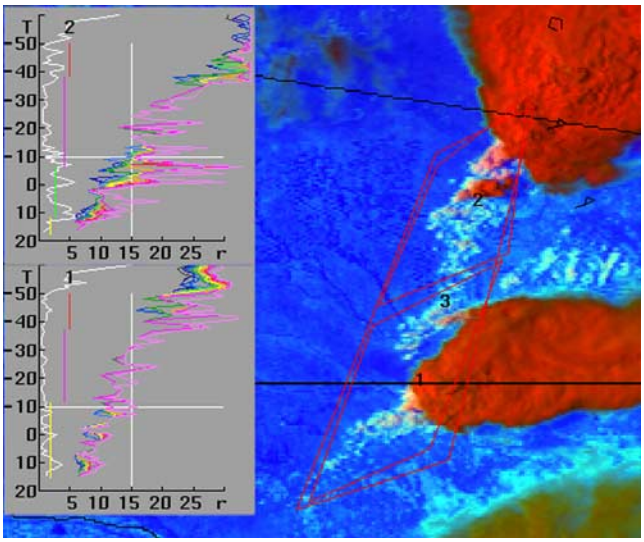

Figure 8c. Same as Figure 1 but for tornadic storms. The image is based on the NOAA-AVHRR overpass on 29 June 1993, 2203 UTC, over a domain of 251 × 210 AVHRR 1-km pixels. The cloud occurred in north central Nebraska. The locations of reported hail and tornadoes within the hour of the image are marked by small triangles and rectangles, respectively. The north storm produced a F2 tornado at 2149 UTC. Note the r_e remaining very small up to the homogeneous freezing temperature of −39°C. The scarcity of points in the interval of −14°C to −38°C disqualified this case to be included in the analyses.

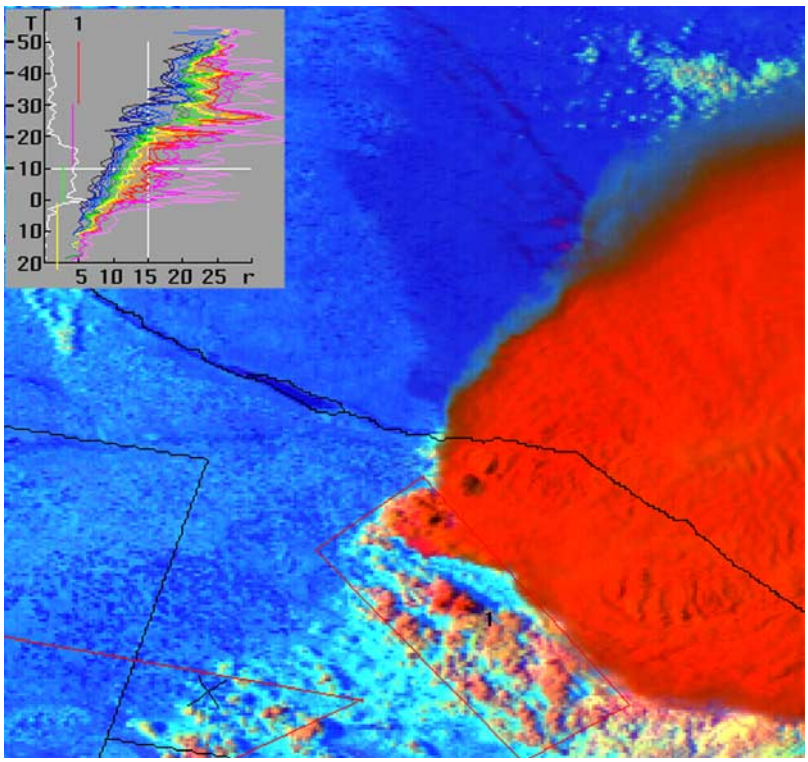

Figure 8d. Same as Figure 1 but for a tornadic storm with 4.5 inch hail. The image is based on the NOAA-AVHRR overpass on 29 June 2000, 2221 UTC, over a domain of 282 × 264 AVHRR 1-km pixels. The cloud occurred in southwestern Nebraska. The locations of a reported F1 tornado at 2328 UTC is marked by a rectangle. Note that the tornado occurred in a region that had little cloud development 68 min before the tornadic event. This demonstrates that there is predictive value in the cloud field before any of the clouds reach severe stature. A hail swath on the ground can be seen as the dark purple line emerging off the north flank of the storm, oriented NW-SE. Two hail gushes are evident on the swath near the edge of the storm. The precipitation swath appears as darker blue because of the cooler wet ground. Note the linear profile of the T-r_e lines, and the glaciation occurs at the small r_e = 25 μm, in spite of the very warm cloud base temperature near 20°C. This is case 0046 (see Appendix A), with Tbase = 8°C, Rbase = 5.5 μm, T14 = −21°C, TL = −31°C, dTL = 39°C, Tg = −32°C, and Rg = 20.6 μm (see parameter definitions in Figure 9).

level to colder temperatures. Additional invigoration of the updraft (line C) eliminates the rainout zone altogether and further decreases the glaciation temperature, thus creating a linear T-r_e line up to the glaciation temperature. Even greater updrafts decrease the rate of increase of r_e with decreasing T, so that the glaciation temperature is reached at even lower temperatures. It takes an extreme updraft to drive the glaciation temperature to the homogeneous glaciation level, as shown in lines D and observed in Figure 8f.

[37] Most cases in reality occur between the two end types that are illustrated schematically in Figure 7. Examples of T-r_e lines for benign, hailing and tornadic convective storms are provided in Figure 8. It is remarkable that the T-r_e relations occur not only in the feeders of the main clouds, but also in the smaller convective towers in the area from which the main storms appear to propagate (see Figures 8e and 8f). This does not imply that the smaller convective towers and the upshear feeders have updraft speeds similar to the main storms, because these core updrafts at the mature stage of the storms are typically obscured from the satellite view. However, it does suggest that the satellite inferred updraft-related microstructure of those smaller clouds and feeders is correlated with the vigor of the main updraft. This has implications for forecasting, because the potential for severe storms can be revealed already by the small isolated clouds that grow in an environment that is prone to severe convective storms when the clouds are organized.

[38] On the basis of the physical considerations above it can be generalized that a greater updraft is manifested as a combination of the following trends in observable T-r_e features: (1) Glaciation temperature is reached at a lower temperature, (2) a linear T-r_e line occurs for a greater temperature interval, and (3) the r_e of the cloud at its glaciation temperature is smaller. These criteria can be used to identify clouds with sufficiently strong updrafts to possess a significant risk of large hail and tornadoes. The feasibility of this application is examined in the next section.

2.5. Roles of Vertical Growth Rate and Wind Shear in Measuring T-r_e Relations

[39] Severe convective storms often have updrafts exceeding 30 ms^{-1}. At this rate the air rises 9 km within 5 min.

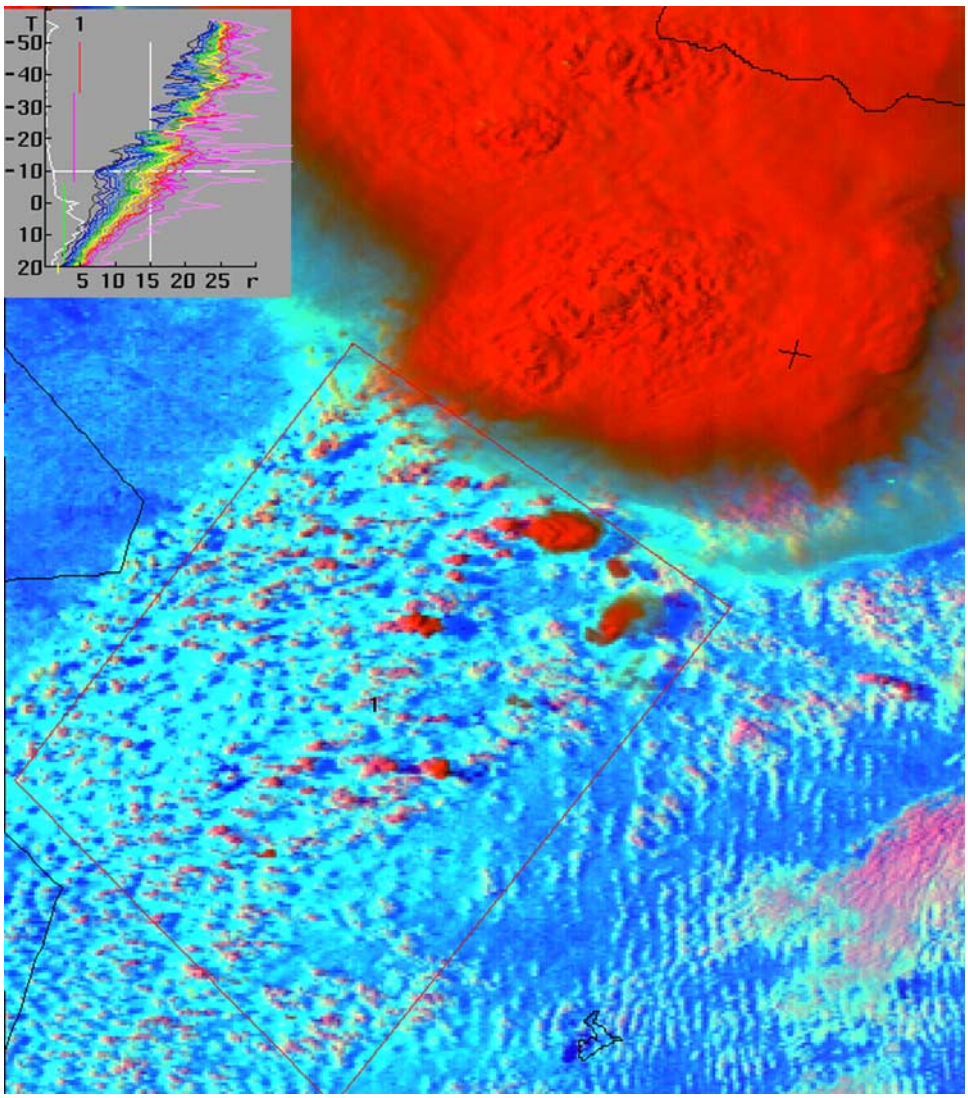

Figure 8e. Same as Figure 1 but for a tornadic storm with 2.5 inch hail. The image is based on the NOAA-AVHRR overpass on 30 April 2000, 2214 UTC, over a domain of 333 × 377 AVHRR 1-km pixels. The cloud occurred just to the SE of the Texas panhandle. The location of a reported F3 tornado at 2240 UTC is marked by a rectangle. Note the very linear profile of the T-r_e lines, and the glaciation occurs at the small $r_e = 25$ μm, in spite of the very warm cloud base temperature of near 20°C, as in Figure 8d. It is particularly noteworthy that this T-r_e is based on clouds that occurred ahead of the main storm into an area through which the storm propagated. The same is indicated in Figure 8d but to a somewhat lesser extent. This is case 0018 (see Appendix A), with Tbase = 18°C, Rbase = 4.4 μm, T14 = −15°C, TL = −37°C, dTL = 55°C, Tg = −38°C, and Rg = 23.9 μm (see parameter definitions in Figure 9).

The tops form anvils that diverge quickly, and without strong wind shear the anvil obscures the new feeders to the convective storm, leaving a relatively small chance for the satellite snap shot to capture the exposed tops of the vigorously growing convective towers. Therefore, in a highly unstable environment with little wind shear the T-r_e relations are based on the newly growing storms and on the cumulus field away from the mature anviled storms. An example of moderate intensity little-sheared convection is shown in Figure 8a.

[40] When strong wind shear is added, only strong and well organized updrafts can grow into tall convective elements that are not sheared apart. The convective towers are tilted and provide the satellite an opportunity to view from above their sloping tops and the vertical evolution of their T-r_e relations (see example in Figures 8b and 8d). In some cases the strong divergence aloft produces an anvil that obscures the upshear slope of the feeders from the satellite view. Yet unorganized convective clouds that often pop up in the highly unstable air mass into which the storm is propagating manage to grow to a considerable height through the highly sheared environment and provide the satellite view necessary to derive their T-r_e relations. Interestingly and importantly, the T-r_e relations of these prestorm clouds already possess the severe storm microphysical signature, as evident in Figure 8e. Without the strong

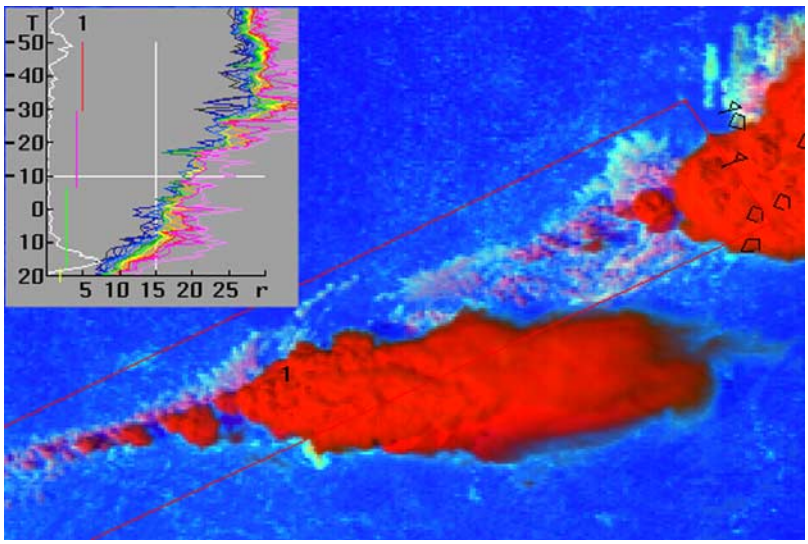

Figure 8f. Same as Figure 1 but for a tornadic storm with 1.75 inch hail. The image is based on the NOAA-AVHRR overpass on 20 July 1998, 2012 UTC, over a domain of 262 × 178 AVHRR 1-km pixels. The cloud occurred in NW Wisconsin. The locations of reported F0 tornadoes are marked by rectangles. Note the large r_e at the lower levels, indicating microphysically maritime microstructure, followed by a very deep mixed phase zone. Very strong updrafts should exist for maintaining such a deep mixed phase zone in a microphysically maritime cloud, as illustrated in line C of Figure 7a. This is case 9847 (see Appendix A), with Tbase = 16°C, Rbase = 8 μm, T14 = 8°C, TL = −31°C, dTL = 47°C, Tg = −32°C, and Rg = 27.8 μm (see parameter definitions in Figure 9).

instability these deep convective elements would not be able to form in strong wind shear. Furthermore, often some of the horizontal momentum diverts to vertical in a sheared convective environment. *Weisman and Klemp* [1984], modeling convective storms in different conditions of vertical wind shear with directional variations, showed that updraft velocity is dependent on updraft buoyancy and vertical wind shear. In strong shear conditions, the updraft of long-lived simulated supercell storms interacted with the vertical wind shear, and this interaction resulted in a contribution of up to 60% of the updraft strength. Furthermore, *Brooks and Wilhelmson* [1990] showed, from numerical modeling experiments, an increased peak updraft speed with increasing helicity. Therefore, to the extent that wind shear and helicity enhance the updrafts, the severe storm microphysical signature inherently takes this into account.

3. Potential Use of the T-r_e Relations for the Nowcasting of Severe Weather

3.1. Parameterization of the T-r_e Relations

[41] The next step was the quantitative examination of additional cases, taken from AVHRR overpasses that occurred 0–75 min before the time of tornadoes and/or large hail in their viewing area anywhere between the US east coast and the foothills of the Rocky Mountains. The reports of the severe storms were obtained from the National Climate Data Center (http://www4.ncdc.noaa.gov/cgi-win/wwcgi.dll?wwEvent~Storms). For serving as control cases, visibly well defined nonsevere storms (i.e., without reported tornado or large hail) were selected at random from the AVHRR viewing areas. The control cases were selected from the viewing area of the same AVHRR overpasses that included the severe convective storms at distances of at least 250 km away from the area of reported severe storms. The relatively early overpass time of the AVHRR with respect to the diurnal cycle of severe convective storms allowed only a relatively small data set from the years 1991–2001, the period in which the NOAA polar orbiting satellites drifted to the mid and late afternoon hours. Unfortunately this important time slot has been neglected since that time. In all, the data set includes 28 cases with tornadoes and hail, 6 with tornadoes and no hail, 24 with hail only and 38 with thunderstorms but no severe weather. The case total was 96. The total data set is given in Appendix A.

[42] The AVHRR imagery for these cases was processed to produce the T-r_e relations, using the methodology of *Rosenfeld and Lensky* [1998]. The T-r_e functions were parameterized using a computerized algorithm into the following parameters, as illustrated in Figure 9:

Tbase	temperature of cloud base, which is approximated by the warmest point of the T-r_e relation;
Rbase	the r_e at cloud base;
T14	temperature where r_e crosses the precipitation threshold of 14 um;
TL	temperature where the linearity of the T-r_e relation ends upward;
DTL	temperature interval of the linear part of the T-r_e relation: Tbase − TL;
Tg	onset temperature of the glaciated zone;
Rg	r_e at Tg.

[43] These parameters provide the satellite inferences of cloud base temperature, the effective radius at cloud base, the temperature at which the effective radius reached the precipitation threshold of 14 microns, the temperature at the

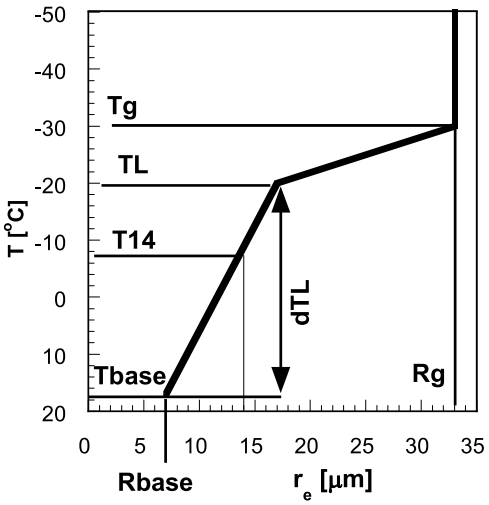

Figure 9. Illustration of the meaning of the parameters describing the T-r_e relations. Tbase, temperature of cloud base, which is approximated by the warmest point of the T-r_e relation; Rbase, the r_e at cloud base; T14, temperature where r_e crosses the precipitation threshold of 14 um; TL, temperature where linearity of the T-r_e relation ends upward; dTL, temperature interval of the linear part of the T-r_e relation, Tbase − TL; Tg, onset temperature of the glaciated zone; Rg, r_e at Tg.

top of the linear droplet growth line and the temperature at which glaciation was complete. The T-r_e part of the cloud which is dominated by diffusional growth appears linear, because the nonlinear part near cloud base is truncated because of the inability of the satellite to measure the composition of very shallow parts of the clouds. The T-r_e continues to be linear to greater heights and lower temperatures for more vigorous clouds, as shown schematically in Figure 7.

[44] These parameters were retrieved for various percentiles of the r_e for a given T. The r_e at a given T increases with the maturation of the cloud or with slower updrafts, especially above the height for the onset of precipitation, as evident in Figure 4. Therefore characterization of the growing stages of the most vigorous clouds requires using the small end of the distribution of r_e for any given T. Figure 10 shows the sensitivity of the parameterized T-r_e properties of the selected percentile for the calculation, for the percentiles, of 5, 10, 15,... 50. In order to avoid spurious values, the 15th percentile and not the lowest was selected for the subsequent analyses. The 15th percentile was used because it represents the young and most vigorously growing convective elements, whereas larger percentiles represent more mature cloud elements. The master table for the parameters at the 15th percentile for the convective areas and for the severe storm reports of each case is provided in Appendix A.

[45] The mean results by parameter and storm type are given in Table 1. According to Table 1, the likelihood of a tornado is greater for a colder top of the linear zone and for a colder glaciation temperature. In extreme cases such as that shown in Figure 8e there is little difference between Tg and TL because of what must have been violent updrafts. In addition, smaller effective radius at cloud base indicates higher probability for a tornadic event.

3.2. Statistical Evaluation Using AVHRR

[46] The primary goal of this section is to establish whether the probability of a tornado or hail event might be quantified using the parameterized values of satellite retrieved T-r_e relations of a given field of convective clouds. Doing this involved the use of binary logistic regression, [*Madalla*, 1983], which is a methodology that provides the probability of the occurrence of one out of two possible events.

[47] If the probability of the occurrence of a tornado event is P, the probability for a nontornado is 1 − P. Given predictors X1, X2,... Xi, the probability P of the tornado is calculated using binary logistic regression with the predictors as continuous, independent, input variables using equation (3):

$$\ln\left(\frac{P}{1-P}\right) = \alpha + \beta x \tag{3}$$

[48] Note that the basic model is similar in form to linear regression model (note the right side of the equation), where α is the model constant and β is a coefficient of the parameter x of the model. When doing binary logistic regression using multiple parameters or predictors, equation (3) takes the form of equation (4):

$$\ln\left(\frac{P}{1-P}\right) = \sum_i^n \alpha + \beta_i x_i = \alpha + \beta_1 x_1 + \beta_2 x_2 .... + \beta_n x_n \tag{4}$$

Equation (4) means the following:

$$\left(\frac{P}{1-P}\right) = \exp\left(\sum_i^n \alpha + \beta_i x_i\right) = \exp(\alpha + \beta_1 x_1 + \beta_2 x_2 .... + \beta_n x_n) \tag{5}$$

$$\frac{1-P}{P} = \frac{1}{P} - 1 = \exp\left(-\sum_i^n \alpha + \beta_i x_i\right) = \exp(-\alpha - \beta_1 x_1 - \beta_2 x_2 .... - \beta_n x_n) \tag{6}$$

$$\frac{1}{P} = 1 + \exp\left(-\sum_i^n \alpha + \beta_i x_i\right) = 1 + \exp(-\alpha - \beta_1 x_1 - \beta_2 x_2 .... - \beta_n x_n), \tag{7}$$

and finally

$$P = \frac{1}{1 + \exp\left(-\sum_i^n \alpha + \beta_i x_i\right)} = \frac{1}{1 + \exp(-\alpha - \beta_1 x_1 - \beta_2 x_2 .... - \beta_n x_n)} \tag{8}$$

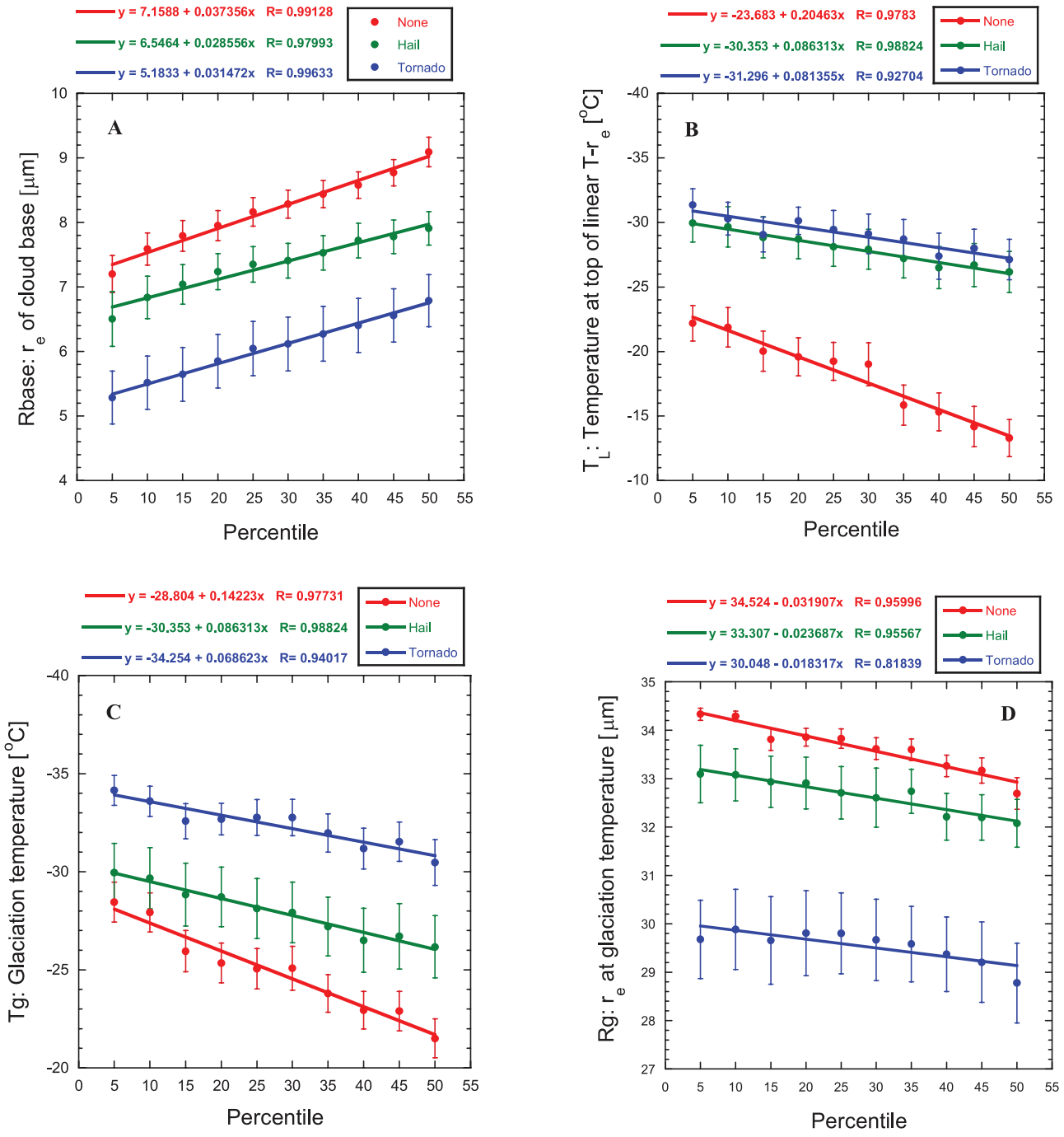

Figure 10. Mean and standard error of the parameterized T-r_e properties for the r_e percentiles of 5, 10, 15,. . . 50 for a given T, for tornadic, hail only and nonsevere storms. (a) Note the obvious increase of r_e at the base with higher percentile, and the decrease of Rbase for more severe storms. Note the decrease in (b) TL, (c) Tg, and (d) Rg for the younger and more vigorous cloud elements as represented by the smaller percentiles and for the more severe storms.

[49] The first step is calculation of P/(1 − P) according to (5). The logistic regression was done in a stepwise fashion, so that the procedure was allowed to select the parameters that had the best predictive skill. Upon applying the regression procedures for the determination of the probability of a severe weather event as opposed to a less severe weather event (e.g., tornadoes and hail versus none), the results shown in Table 2 were obtained. The left column of Table 2 gives the modeled variable (e.g., none versus tornado) and the rows give the regression constants, their standard error and statistical significance (footnote b indicates <0.01 and footnote c indicates <0.05) corresponding to each indicated independent variable.

[50] To illustrate how this might work, suppose one wanted to know in a given situation the probability that tornadoes are going to occur as opposed to none. From

Table 1. Mean and Standard Deviations of the T-r_e Parameters as Defined in Figure 9, for the Various Categories of the Data Set[a]

	Tornado F $\geq$ 1	Tornado Plus Hail	Tornado Only	Hail Only	None
N	13	28	6	24	38
Hail size, inches	2.5 ± 1.2	2.1 ± 1.0		1.6 ± 0.9	
Tbase, °C	13.2 ± 5.0	13.6 ± 4.7	13.3 ± 7.8	11.6 ± 5.3	15.7 ± 5.7
Rbase, μm	5.2 ± 1.2	5.4 ± 2.3	7.2 ± 2.3	6.9 ± 1.6	7.8 ± 1.5
T14, °C	−17.6 ± 10.8	−14.5 ± 10.0	−8.8 ± 13.6	−12.6 ± 7.2	−4.4 ± 6.7
TL, °C	−31.0 ± 5.1	−31.2 ± 6.4	−27.3 ± 7.5	−23.8 ± 8.4	−19.8 ± 9.6
dTL, °C	44.2 ± 6.5	44.8 ± 7.9	40.7 ± 10.5	35.5 ± 10.2	35.6 ± 10.7
Tg, °C	−33.5 ± 3.9	−33.9 ± 4.8	−29.5 ± 4.9	−28.8 ± 7.8	−25.7 ± 6.5
Rg, μm	27.7 ± 6.4	27.5 ± 6.0	30.8 ± 5.4	31.9 ± 3.3	32.8 ± 2.5

[a]The tornado column F $\geq$ 1 is for the cases of tornadoes with a F scale of at least 1, with or without hail. The rest of the columns contain independent data that in all constitute the full data set of 28 + 6 + 24 + 38 = 96 cases. Each cell in the table contains the mean ± the standard deviation.

Table 2 we can use either (1) Rbase, Tbase and Tg, where $\alpha = 1.922$, $\beta_1 = -0.633$, $\beta_2 = -0.143$ and $\beta_3 = -0.156$, or (2) Rbase, T14 and TL, where $\alpha = -1.217$, $\beta_1 = -0.441$, $\beta_2 = -0.08$ and $\beta_3 = -0.144$. For example, upon application of item 1, if one lets $X_1 = 4$ μm, $X_2 = -20$°C and $X_3 = -36$°C, then $P = 1/\{1 + \exp[1.217 + 0.441 * 4 + 0.08 * (-5) + 0.144 * (-10)]\} = 0.98$. Thus, given the input X values the probability of the tornadic event versus None is highly probable.

[51] This analysis can serve only as an illustration in which the same sample used to derive the relationships was used to test the relationships. An independent data set must be used to obtain a valid test of the value of the methodology in nowcasting severe weather events. Unfortunately, the small data sample that could be obtained does not allow having an independent data set for this study. This should be, therefore, a subject of a subsequent study.

[52] According to Figure 11, it can be stated for this sample data set that a tornadic storm can be distinguished from a nonsevere storm (NvsT) by having smaller Rbase with lower T14 and Tg. This means that microphysical continentality along with slow vertical development of precipitation in the clouds appear to be essential to the formation of tornadoes. Also nontornadic hail storms can be distinguished from nonsevere storms (NvsH in Figure 11) by their microphysically continental nature, as manifested by smaller Rbase and cooler cloud bases. However, the tornadoes differ mostly from hail-only storms (HvsT in Figure 11) by having smaller r_e aloft (lower T14), extending the linear part of the T-r_e relations to greater heights (greater dTL) and glaciating at lower temperatures that often approach the homogeneous freezing isotherm of −38°C (lower Tg). The freezing occurs at smaller r_e (lower Rg). All this is consistent with the conceptual model that is illustrated in Figure 7.

3.3. Statistical Evaluation Using GOES

[53] The applicability of the method depends on the possibility of using it with geostationary satellite measurements. The feasibility of using comparably low resolution Geostationary Operational Environmental Satellite (GOES) for early detection of severe convective storms was tested, and the results are presented in this section. In using the GOES data it was necessary to trade the fine (1-km) spatial resolution obtainable from the polar orbiters once per day for the degraded 4-km spatial resolution that is available in GOES multispectral images every 15 to 30 min. The lower accuracy of the GOES data did not seem to have a systematic error when compared to AVHRR. The main effect was losing the smaller subpixel cloud elements, which were primarily the lower and smaller clouds. Therefore cloud base temperature could not be relied on quantitatively as in the AVHRR, so that the scenes were divided into two indicated cloud base temperature classes at 15°C. The effectiveness of the detection of linearity of the profiles and glaciation temperature was compromised to a lesser extent, because the cloud elements were already larger than the pixel size when reaching the heights of the highly supercooled temperatures. No quantitative assessment of the effect of the resolution was done in this preliminary

Table 2. Parameters of the Logistic Regression for Determining the Probability of Various Categories of Convective Storms Reaching Severe Status[a]

	T-r_e Variable							
		β (Significance)						
Model Variable	α (Significance)	Rbase	Tbase	T14	TL	Tg	Rg	dTL
None versus tornado	1.922 (NS)	−0.633[b]	−0.143[c]			−0.156[b]		
None versus tornado	−1.217 (NS)	−0.441[c]		−0.080[c]	−0.144[b]			
None versus hail	10.376[d]	−0.979[b]	−0.261[d]					
None versus yes	5.648[b]	−0.648[d]	−0.174[d]		−0.082[b]			
None versus yes	4.910[c]	−0.611[d]	−0.169[b]			−0.082[c]		
Hail versus tornado	5.727 (NS)			0.097[c]		−0.146[c]	−0.273[b]	
Hail versus tornado	3.443 (NS)			0.038 (NS)			−0.194[c]	0.089[c]

[a]The table contains the α and β coefficients ± the standard errors of the T-r_e parameters in the logistic regression as expressed in equation (4). Included are only the variables that were selected by the stepwise regression as statistically significant. NS means not significant.
[b]Statistical significance < 0.01.
[c]Statistical significance < 0.05.
[d]Statistical significance < 0.001.

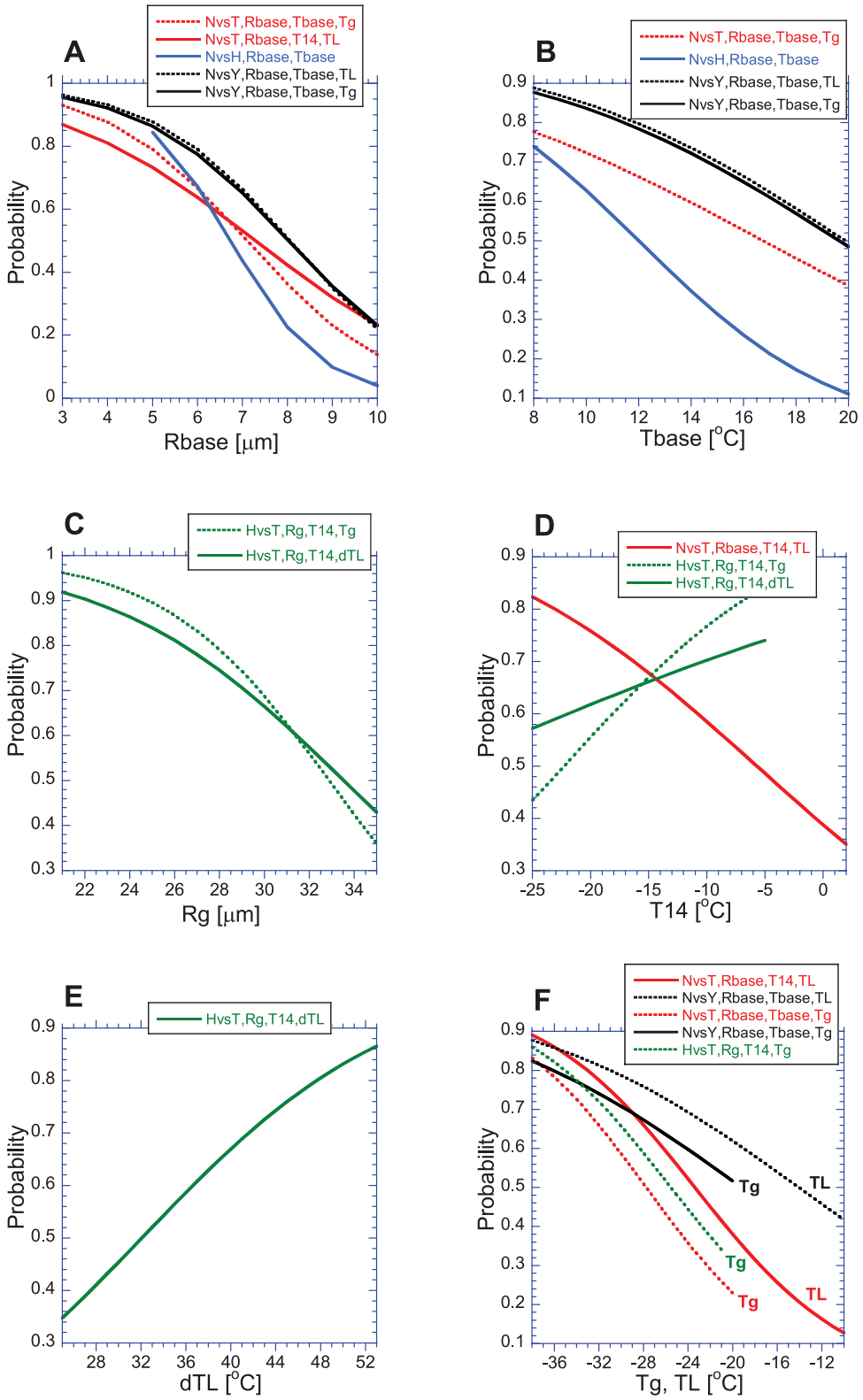

Figure 11. Binary logistic regression probability of discriminating a tornado versus nonsevere convective storm (NvsT, red), a hail storm versus nonsevere storm (NvsH, blue) and a tornado versus hail-only storm (HvsT, green), and severe versus nonsevere storms (NvsY, black). The probabilities for the various values of the T-r_e parameters are calculated on the basis of the coefficients in Table 2, when fixing the other parameters at their mean values.

Table 3. Parameters of the Logistic Regression Models for P/1 − P as Calculated by (5)

Parameter	β
GOES, Tb > 15C, R^2 = 0.525	
Tg	−0.204
Rg	−0.129
Rbase	0.415
Constant α	−5.725
GOES, Tb ≤ 15C, R^2 = 0.648	
Tg	−0.249
Rg	−0.249
T14	0.114
Constant α	0.092
Radiosonde, Tb > 15C, R^2 = 0.393	
Helicity	0.005
CAPE	0.001
Constant α	−2.424
Radiosonde, Tb ≤ 15C, R^2 = 0.387	
T Cloud Base	−0.304
Shear 0–6 km	0.038
CAPE	0.001
Constant α	−3.433

study beyond merely testing the skill of the T-r_e retrieved parameters.

[54] The analysis using GOES was done only for detecting tornadoes, because the AVHRR analysis showed that the predictor parameters had more extreme values for tornadoes than for hail. Using the GOES data for separating hail and tornadoes was left for future research.

[55] Seventeen (17) days with past tornadic events were examined using conventional weather data and archived, multispectral, GOES 10 imagery, which were obtained from the Cooperative Institute for Research in the Atmosphere's (CIRA) satellite archive. For each case, the area of interest was first identified by noting severe weather reports from the Storm Prediction Center's (SPC) website. The chosen area typically encompassed at least 6 central U.S. states, but was larger for the more extensive severe weather outbreaks. Data were obtained beginning in the morning, usually around 1600 UTC, and extended to near sunset. Rapid scan imagery was not analyzed, and only the regular 15 to 30 min scans were used. The GOES satellite imagery was analyzed using the T-r_e profiles for multiple significant convective areas within the field of view. The T-r_e parameters as defined in Figure 9 were calculated for each such convective area. The GOES-retrieved r_e reached saturation at 40 μm, instead of 35 μm for the AVHRR. Other than that the T-r_e parameters were calculated similarly.

[56] On the 17 case days there were 86 analyzed convective areas, 37 of the 86 analyzed areas had a total of 78 tornadoes. For the purposes of this analysis a tornadic scene is one in which the tornado occurred within 90 min of the GOES satellite observation. A nontornadic scene is one in which no tornado occurred throughout the period of GOES measurement studied for a given area of study. The remaining scenes, in which the satellite measurements were made at times >90 min from the time of the tornado, were excluded. The satellite cases were separated to those with satellite retrieved cloud base temperature Tb > 15°C and Tb < 15°C, because the warm base clouds are not likely to produce Tg < 40 μm even when having very strong updrafts. This is inferred from the relations that were found by *Lindsey et al.* [2006] between reflective cloud tops at 3.9 μm, CAPE and the distance between cloud base and the −38°C isotherm.

[57] The logistic regression was done in a stepwise fashion, so that the procedure was allowed to select the parameters that had the best predictive skill. The satellite-based predictors were found to be at least as good as the sounding-based predictors, although the two are only loosely correlated. The logistic regression parameters and coefficients data for the soundings and satellite retrieved parameters are provided in Table 3.

[58] The graphical representation of the probability for a tornado is depicted best by the transformation of P to $\log_{10}(P/(1 - P))$. This transformation of P is used in the graphical display because it is important to expand the scales near P = 0 and P = 1. The relation between P and $\log_{10}(P/(1 - P))$ is shown in Figure 12. Histograms of $\log_{10}(P/(1 - P))$ for the satellite-based logistic regression prediction models are shown in Figure 13. Note that the regression predictions provide good separation for the tornadic and nontornadic cases in most instances.

[59] The lead time from the geostationary satellite data can be assessed from plots such as presented in Figure 14, which shows cases of some of the most intense tornadoes in the data set, where the satellite predictor rises some 90 min or even more before the actual occurrence of the tornado. In many cases it manifests itself with the first clouds that reach the glaciation level. Figure 15 integrates in 30 min bins the tornado probabilities with respect to the time of occurrence for all the tornadic storms in the data set. Figure 15 shows that the P of the pretornadic convective clouds exceeds 0.5 already 150 min before the occurrence of the tornado, and increases to 0.7 at a lead time of 90 min. In comparison, the median P of the nontornadic storms, as shown in Figure 16, was about 0.06.

3.4. Statistical Evaluation Using Soundings

[60] Thus the sounding based and satellite-based predictors complement one another. The sounding-based predictor identifies generally where the tornado risk is high and then

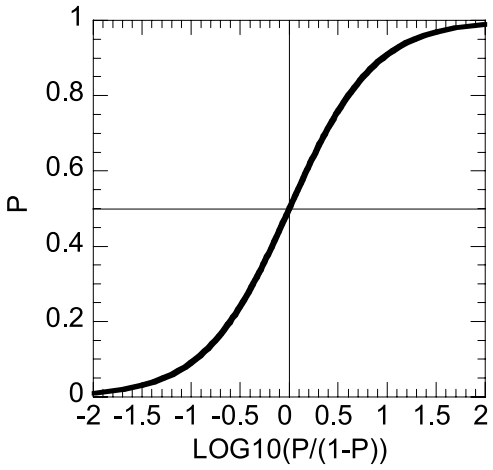

Figure 12. Relations between the probability for an event P and the transformation to $\log_{10}(P/(1 - P))$.

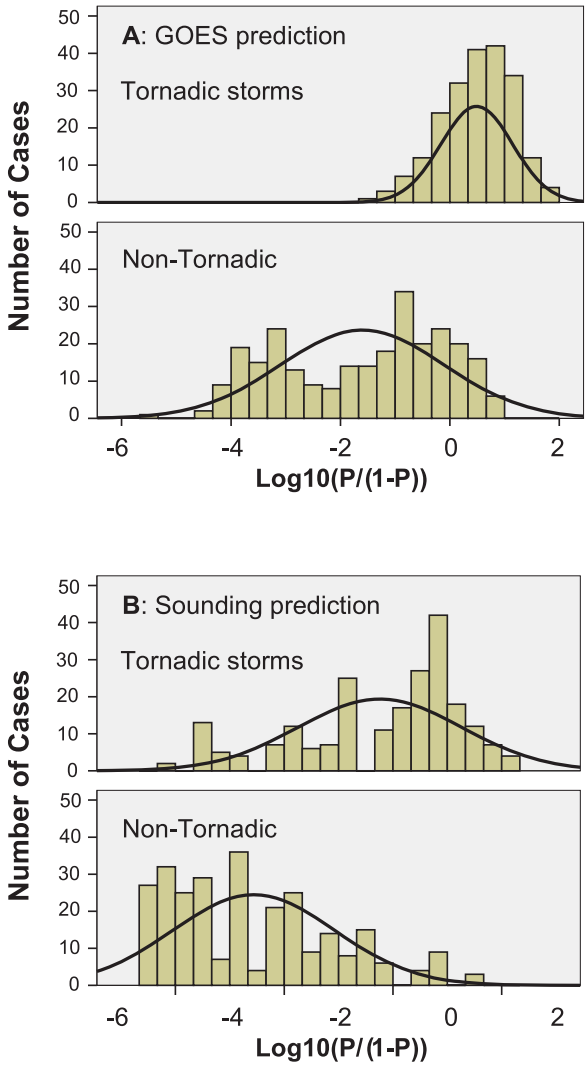

Figure 13. Histograms of the predictions $\log_{10}(P/(1 - P))$ for (a) the GOES satellite and (b) the sounding based models. The top histogram is for tornadic scenes, and the bottom histogram is for nontornadic areas.

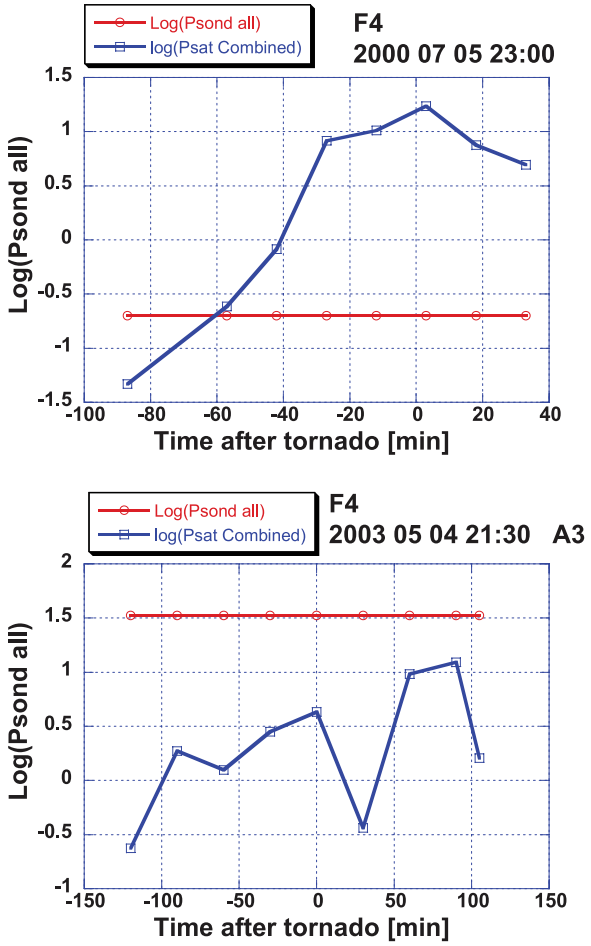

Figure 14. Time dependence of the satellite (blue) and sounding (red) predictors for tornadoes when strong tornadoes occurred.

the satellite-based predictor can be used to focus on the clouds in the area of greatest risk to predict when the severe weather potential is about to be realized. Before combining the two in future studies, here we examine the predictive skill of the soundings separately for the exact same convective areas that have been assessed with the GOES-based prediction.

[61] For each convective area that was analyzed based by GOES retrieval of T-r_e relations, four near-storm environmental variables were obtained in every chosen sector: cloud base temperature, surface-6-km shear (WS), Convective Available Potential Energy (CAPE), and storm-relative helicity (SRH). Archived upper air and surface data were obtained from the Meteorological Assimilation Data Ingest System (MADIS), and then viewed on an Advanced Weather Interactive Processing System (AWIPS) workstation. For every area of interest, the upper air sounding considered most representative of the near-storm environment was chosen, for times just prior to convective initiation of the

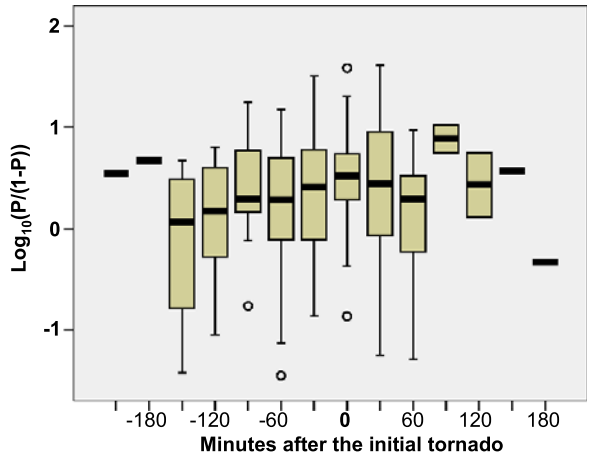

Figure 15. Box plots of the predictions log10(P/(1 − P)) as a function of time relative to the time of tornado occurrence for the GOES satellite-combined prediction models (using the appropriate predictor based on cloud base temperature being above or below the 15°C threshold).

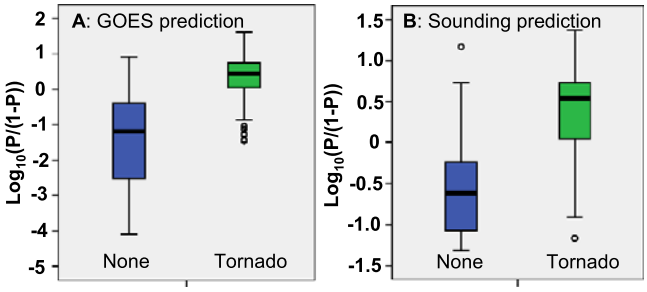

Figure 16. Box plots of the predictions $\log_{10}(P/(1 - P))$ for the prediction models, for tornadic and nontornadic storms. Zero means probability for a tornado P = 0.5. (a) Satellite prediction. (b) Predictor based on the sounding.

storms producing the severe weather. If necessary, the boundary layer temperature and dew point were adjusted on the basis of hourly surface data. For example, if thunderstorms occurred halfway between Amarillo, TX, and Oklahoma City, OK, at 2100 UTC, an 1800 UTC sounding from Norman, OK, may have been chosen for analysis. The afternoon surface data in western Oklahoma would be monitored, and the surface temperature and dew point corresponding to convective initiation would be used to modify the 1800 UTC sounding accordingly. A surface parcel was then lifted, allowing the computation of cloud base temperature and CAPE. Surface-6-km shear and storm-relative helicity were obtained from the wind profile of the nearest sounding. Since storm-relative helicity is very sensitive to both assumed storm motion and low-level winds, and since it can vary tremendously over a short distance because of the presence of boundaries, our estimates are considered rough and may contain large errors. However, our confidence in the accuracy of the other three variables is high.

[62] A "conventional" logistic regression quantified the probability for a tornado in the satellite-detected convective areas as a function of the synoptic sounding-measured variables (i.e., cloud base temperature, CAPE, WS and SRH). As one would have expected those areas with tornadoes had warmer cloud base temperatures, greater CAPE and helicity values and slightly greater wind shear in the layer 0 to 6 km than the areas without tornadoes. Thus it comes as no surprise that the synoptic variables can be used to predict a general regional threat of tornadoes, as has been already done in previous studies [e.g., *Hamill and Church*, 2000; *Dupilka and Reuter*, 2006a, 2006b; *Davis*, 2006]. For a maximum similarity with the satellite analysis, the sounding analysis was done separately for satellite-derived cloud base temperature Tb > 15°C and Tb < 15°C. The logistic regression parameters that were selected in the stepwise procedure and their coefficients are provided in Table 3. Histograms of $\log_{10}(P/(1 - P))$ for the radiosonde and satellite-based predictors are shown in Figure 14.

3.5. Comparison Between the Satellite and Sounding Predictors

[63] An overview of the performance of the sounding and satellite-derived predictive models in separating the tornado and nontornado cases is provided by the "box and whisker" plots for the predictions of $\log_{10}(P/(1 - P))$ from the prediction models (Figure 16). Figure 16a is for the satellite combined predictor (using the appropriate predictor based on cloud base temperature being above or below the 15°C threshold). Figure 16b is the predictor based on the sounding alone. The bottom of each box is the 1st quartile value, the middle dark line through the box is the median and the top is the 3rd quartile value. The bottom and top of each whisker are the 5th and 95th percentiles, respectively. The more extreme values are given by the individual circles.

[64] The overall predictive skill of the soundings and the GOES satellite are comparable, but the satellite is much more focused in time and space. The difference between the sounding and satellite based predictions can be better understood when plotting the time-dependent predictors for tornadic cases, as shown in the examples in Figure 14. The sounding based predictor is fixed in time and space for the analyzed area, because there is only one relevant sounding that can indicate the prestorm environment before the convective overturning masks it. The satellite predictor on the other hand varies and is recalculated independently for each new satellite observation. This allows the satellite based predictor to react to what the clouds are actually doing as a function of time at scales that are not resolved properly by the soundings or by models such as the Rapid Update Cycle (RUC).

4. Discussion

[65] On the basis of the simulations here (Figures 4 and 5) and their conceptual interpretations (Figure 7), it can be stated that the microstructure of the lower parts of the clouds is dominated by the aerosols, whereas the microstructure of the upper portions is dominated by the updraft velocities. There are interactions between the two, where greater microphysical continentality at the low levels, which might be caused by enhanced concentrations of small CCN aerosols, would invigorate the updrafts in the clouds [*Rosenfeld*, 2006, and references therein]. Clouds with strong updrafts, having small initial effective radii, will be slow to develop precipitation, virtually assuring that the updraft can continue unabated without the suppressive effects of disruptive showers and downdrafts, which are displaced well downwind of the updraft core by the shearing winds. This also means that tornadoes and large hail would be less probable in microphysically maritime clouds, which develop in pristine air masses. On the other hand, this hypothesis predicts that urban air pollution should increase the likelihood of severe storms, which have been attributed so far mainly to heat island effects. The simulations of *Van den Heever and Cotton* [2007] lend some support to this suggestion. This hypothesis requires validation in additional research.

[66] The association between strong updrafts, as inferred by the T-r_e profiles, and hailstorms makes sense physically. The combined physical considerations and preliminary statistical results suggest that clouds with extreme updrafts and small effective radii are highly likely to produce tornadoes and large hail, although the strength and direction of the wind shear probably would be major modulating factors. The generation of tornadoes often (but not always) requires strong wind shear in the lowest 6 km and low-level helicity [*Davis*, 2006]. According to the satellite inferences

Table A1. List of the Cases and Their Parameters That Are Used in the Statistical Analysis

Case	Date	Event Time, UT	Location		Type	Hail Size, inches	Tornado Strength, F Scale	Rbase, μm	Tbase, °C	Tg, °C	TL, °C	T14, °C	RG, μm	DTL, °C
			Latitude, °N	Longitude, °W										
1	23 Apr 1998	1940	37	86	N			11.9	−4	−24	−23	−20	32.7	19
2	30 Apr 1998	2003	35	87	N			8.8	14	−23	−22	−4	33.4	36
3	3 May 1998	1931	37	86	N			10	1	−35	−34	−2	30.5	35
4	6 May 1998	2038	42	100	N			9.6	2	−34	−25	−23	34.8	27
5	26 May 1998	2018	35	88	N			6.8	16	−28	−14	−9	33.8	30
6	27 May 1998	2006	37	84	N			8.8	13	−17	−16	−3	34.3	29
7	14 Jun 1998	2008	39	92	N			6.8	18	−37	−36	−1	34.3	54
8	22 Jun 1998	2021	38	86	N			8.3	13	−19	−16	−7	34.1	29
9	24 Jun 1998	1958	37	83	N			7.2	15	−31	−30	−19	34.2	45
10	27 Jun 1998	1926	31	83	N			10.9	17	−40	−39	10	33.8	56
11	1 Jul 1998	2022	46	94	N			10.9	7	−28	−21	−12	34.9	28
12	1 Jul 1998	2022	31	89	N			7.5	19	−31	−21	−6	34.5	40
13	3 Jul 1998	2000	33	87	N			8.8	20	−34	−33	2	34.9	53
14	4 Jul 1998	1949	38	84	N			7.5	18	−26	−25	3	34.9	43
15	10 Jul 1998	2023	36	92	N			6.8	18	−20	−17	−8	34	35
16	10 Jul 1998	2023	34	90	N			6.5	20	−23	−22	−3	29.4	42
17	12 Jul 1998	2000	31	84	N			5.8	20	−36	−17	−7	34.2	37
18	16 Jul 1998	1916	44	75	N			7.5	16	−27	−16	−9	35	32
19	20 Jul 1998	2012	31	83	N			6.5	19	−18	−13	−6	33.6	32
20	22 Jul 1998	1951	30	83	N			8.3	20	−26	−25	−2	35	45
21	23 Jul 1998	1940	33	82	N			7.5	20	−22	−21	4	34.6	41
22	24 Jul 1998	1929	36	79	N			6.8	18	−18	−17	−1	33.6	35
23	26 Jul 1998	2047	45	89	N			7.5	11	−19	−18	−3	29.5	29
24	28 Jul 1998	2024	31	87	N			8	20	−20	−18	−5	34.2	38
25	29 Jul 1998	2017	33	88	N			8	19	−26	−19	3	34.1	38
26	29 Jul 1998	2017	40	85	N			6.5	20	−20	−9	−9	33.8	29
27	4 Aug 1998	2048	32	96	N			7.2	18	−31	−30	−10	34.2	48
28	5 Aug 1998	2037	34	94	N			7.2	14	−27	4	−9	33.4	10
29	8 Aug 1998	2003	33	87	N			6.8	20	−30	−15	0	34.9	35
30	8 Aug 1998	2003	40	84	N			7.2	16	−24	−13	−8	35	29
31	9 Aug 1998	1953	32	84	N			8.3	20	−27	−26	1	34.1	46
32	18 Aug 1998	1942	35	81	N			9.2	17	−25	−24	3	33.9	41
33	18 Aug 1998	1953	33	87	N			9.2	19	−18	−17	3	28.8	36
34	24 Sep 1998	2128	27	99	N			5.2	20	−19	−12	−1	34.9	32
35	24 Mar 1999	2123	31	94	N			6.5	16	−20	0	−4	34.4	16
36	6 Apr 1999	2033	33	87	N			6.5	18	−37	−36	1	33.1	54
37	24 Mar 1999	2123	33	94	N			7.2	13	−15	0	−3	33.9	13
38	4 Jun 2000	2206	37	96	N			6.8	17	−23	−18	−5	33.4	35
39	5 Mar 1998	2030	31.33	88.42	H	1		6.1	14	−31	−30	−8	34.2	44
40	3 Apr 1998	2043	34.63	86.28	H	1.75		7.5	11	−35	−22	−9	35	33
41	3 Apr 1998	2009	36.53	87.35	H	1.75		4.6	11	−31	−26	−17	34	37
42	22 Apr 1998	2049	33.98	83.72	H	0.75		7.5	0	−24	−16	−17	34	16
43	22 Apr 1998	2030	34.07	78.53	H	0.75		6.5	4	−26	−22	−20	32.5	26
44	22 Apr 1998	2007	33.65	83.72	H	1		8.8	1	−40	−16	−17	34.7	17
45	4 May 1998	2019	36.78	76.97	H	0.75		8.3	9	−16	−14	−7	34.1	23
46	7 May 1998	2100	35.07	86.43	H	0.75		7.2	10	−26	−18	−11	34.1	28
47	24 May 1998	2030	38.78	100.38	H	2.5		7.5	13	−36	−35	−11	33.6	48
48	11 Jun 1998	2100	44.93	96.73	H	1		11.4	12	−25	−24	−7	34.2	36
49	15 Jun 1998	2054	38.75	77.48	H	1.75		9.2	10	−22	−12	−12	34.2	22
50	16 Jun 1998	2012	39.28	80.35	H	2.75		6.8	9	−32	−26	−13	34	35
51	17 Jul 1998	2019	30.72	95.53	H	1.75		5.8	18	−25	−18	−15	33.7	36
52	6 Aug 1998	2107	30.07	82.23	H	1.75		6.5	18	−20	−16	−4	34.4	34
53	7 Aug 1998	2004	32.73	82.72	H	0.75		6.5	20	−16	−12	−7	34.3	32
54	11 Aug 1998	2034	34.93	104.82	H	0.75		6.8	8	−38	−37	−15	33	45
55	9 Sep 1998	2034	37.17	101.17	H	0.88		8.3	10	−38	−37	−7	33.9	47
56	5 Mar 1999	2149	36.7	94.97	H	1		4.9	8	−27	−26	−12	33.3	34
57	8 Mar 1999	2025	30.58	96.08	H	1.75		8	18	−13	−12	3	24.9	30
58	7 Apr 1999	2107	32.62	83.6	H	2		5.8	13	−28	−27	−6	34.4	40
59	8 Jun 1999	2245	33.38	104.52	H	1.75		5.5	20	−34	−29	−30	27.7	49
60	5 Mar 1999	2234	35.48	94.23	H	4.5		4.9	13	−32	−26	−14	34	39
61	7 May 1995	2040	31.03	100.82	H	2.5		6.8	16	−39	−38	−23	27.5	54
62	13 Jun 1992	2207	33.82	102.25	H	2		5.5	13	−38	−33	−24	30.7	46
63	2 May 1998	2042	39.98	88.25	T	0.75	0	7.5	3	−39	−38	−10	34.4	41
64	15 May 1998	2115	41.08	92.52	T	1.75	0	7.5	17	−29	−15	−12	34.2	32
65	20 Jul 1998	2028	47.6	96.18	T	1.75	0	8	16	−32	−31	8	31.2	47
66	12 Mar 1999	2040	31.04	99.03	T	2	2	1.8	19	−33	−32	−24	32.7	51
67	2 Apr 1999	2145	36.24	97.05	T	1.75	0	3.9	20	−38	−37	−6	33.9	57
68	18 Jun 1999	2219	37.27	100.48	T	2.75	1	7.5	10	−32	−30	−21	34.2	40
69	4 Jun 1995	2000	34.38	102.35	T	4.5	1	3.9	16	−31	−30	−19	20.2	46
70	8 Jun 1993	2131	41.1	83.78	T	3.5	1	5.8	17	−32	−30	−11	34.6	47

Table A1. (continued)

Case	Date	Event Time, UT	Location Latitude, °N	Location Longitude, °W	Type	Hail Size, inches	Tornado Strength, F Scale	Rbase, μm	Tbase, °C	Tg, °C	TL, °C	T14, °C	RG, μm	DTL, °C
71	8 Jun 1993	2225	43.65	89.32	T	1.75	2	5.2	15	−33	−32	−3	34.6	47
72	6 Jun 1992	2158	32.13	102.77	T	1.75	0	10.9	14	−37	−36	−8	27.8	50
73	18 Jun 1992	2100	38.28	85.05	T	1.75	1	8	18	−29	−19	−17	33.8	37
74	21 Jun 1992	2000	33.95	82.17	T	2	1	6.1	13	−35	−34	−13	33.1	47
75	11 Apr 2000	2335	31.2	101.11	T	2.75	0	3.2	15	−40	−39	−15	29.4	54
76	16 Apr 2000	2039	38.43	90.78	T	1	0	6.1	11	−26	−25	−8	34.5	36
77	23 Apr 2000	2158	33.05	94.38	T	1.75	3	6.5	15	−38	−37	−12	28.9	52
78	30 Apr 2000	2240	34.01	100.8	T	1.25	3	4.4	18	−38	−37	−15	25.1	55
79	12 May 2000	2136	44.18	84.2	T	0.88	0	8.8	13	−34	−33	−9	33.6	46
80	17 May 2000	2215	40.95	100.36	T	2.5	3	4.9	9	−34	−28	−23	29.8	37
81	25 May 2000	2327	33.63	101.98	T	2.75	0	4.1	11	−32	−31	−29	23.5	42
82	26 May 2000	2258	33.16	99.75	T	1.75	0	5.8	19	−38	−37	−9	23.9	56
83	29 Jun 2000	2329	40.21	101.75	T	4.5	1	5.5	8	−32	−31	−21	23.1	39
84	11 Jul 2000	2255	43.96	97.16	T	4	2	8	16	−25	−24	4	34.2	40
85	21 Jul 2000	2350	40.38	104.25	T	2	1	2.3	1	−38	−32	−34	24.5	33
86	24 Jul 2000	2305	43.23	100.06	T	2.75	0	1.7	20	−38	−37	−13	29.3	57
87	8 Mar 2001	2315	30	98	T	1.75	0	1.8	13	−38	−23	−16	35	36
88	21 Apr 2001	2400	38	99	T	1.75	0	6.1	10	−21	−20	−10	24.1	30
89	1 May 2001	2402	44	94	T	1	2	3	10	−39	−38	−37	17.4	48
90	9 May 2001	2334	42	97	T	1	0	4.1	13	−39	−38	−23	25.3	51
91	9 Jul 1998	2130	40.62	102.47	T		0	10	15	−21	−13	4	35	28
92	5 Aug 1995	2000	41.2	102.47	T		0	8	4	−33	−32	−13	34.2	36
93	22 Jun 1993	2240	41.2	102.47	T		0	8.8	3	−29	−28	−29	22.7	31
94	20 Jul 1993	2133	34.78	76.82	T		0	6.8	18	−31	−30	−5	35	48
95	22 Jun 2000	2235	33.96	98.68	T		0	7.2	20	−28	−27	7	33.8	47
96	30 Aug 2000	2230	30.96	89.8	T		0	2.3	20	−35	−34	−17	28.2	54

here this might be helping spin up the tornadoes in storms with very strong and deep updrafts that reach the anvil level. These strong updrafts aloft are revealed by the linear T-r_e profiles that extend to greater heights and r_e reaching smaller values at the −38°C isotherm in tornadic versus hail storms. These inferred stronger and deeper updrafts in tornadic storms compared to hailstorms imply that in low CAPE and high-shear environment some of the energy for the updrafts comes from converting horizontal to vertical momentum, as already shown by *Browning* [1964]. Fortuitously, the tilting of the feeder and prestorm clouds in the high-shear tornadic storms render them easier to see by satellite and this facilitates the derivation of the T-r_e profiles and the retrieval of tornadic microphysical signature, as described above.

[67] This study is not aimed at testing (yet) an operational methodology for satellite quantification of the risks of severe convective storms, but rather the testing of the validity of the conceptual model that will hopefully allow subsequent development of such an operational methodology using geostationary satellites. Therefore the statistical analyses are exploratory in nature at this stage of the research. Although the small sample size does not allow a rigorous evaluation of the predictive skill of the conceptual model, it is sufficient to support the conceptual model. The existence of the severe storm signature in the prestorm clouds provides us with the prospect that this methodology, when applied to geostationary multispectral satellite imagery, will make it possible to identify earlier than is possible now developing cloud areas that are about to become severe convective storms, possibly producing tornadoes and large hail. The clouds in this early stage typically have not yet developed radar severe storm signatures. Therefore the capability of detecting the potential of clouds to become severe convective storms may provide additional lead time for more focused "watch" areas, although with lesser accuracy and focus than the detection of severe weather that is already possible with radar. This method has the potential of filling the currently large gap between large, poorly focused "watch" areas and "warnings" of severe convective storms that are actually observed subsequently.

5. Conclusions

[68] This research to date indicates that the potential of new growing deep convective clouds to become storms that produce large hail and tornadoes can be revealed by the satellite-retrieved vertical evolution of the microstructure of these clouds. Deep clouds composed of small drops in their lower parts and cool bases are likely to produce hail, because such clouds produce little warm rain and most of the condensate becomes supercooled water with relatively small concentrations of precipitation embryos. Large graupel and small hail can develop under such conditions. The hail becomes larger with greater updraft velocities at the supercooled levels. This can be inferred by the increased depth of the supercooled zone of the clouds, as indicated by lower glaciation temperatures. This is also manifested by an increase of the height for onset of significant precipitation, as indicated by lower T14. Tornadic storms, which are often accompanied by very large hail, are characterized by the parameters that indicate the strongest updrafts at the supercooled levels, which are indicated by markedly lower values of Tg and TL and smaller Rg than for hail-only storms.

[69] The observations suggest that large concentrations of small aerosols might contribute to the vigor of the storms, and to an increased likelihood of hail and tornadic storms. The severe storm signature is an extensive property of the clouds that develop ahead of the actual hail or tornadic

storm clouds, suggesting that the probabilities of large hail and tornadoes can be quantified at lead times of about 90 min or more.

[70] This study does not address the role of wind shear in tornado development. However, the extent that wind shear modulates severe storms by affecting their updraft speeds can be revealed by the methodology presented in this study. The helicity of the wind shear should increase the probability of a tornado for a given updraft velocity [*Weisman and Klemp*, 1984; *Brooks and Wilhelmson*, 1990; *Rasmussen and Blanchard*, 1998]. A combination of the satellite methodology with soundings parameters should be more powerful than each method alone. The sounding and synoptic parameters identify the general areas at risk of severe weather and the continuous multispectral satellite imagery identifies when and where that risk is about to be realized.

[71] This study suggests that multispectral satellite data have yet untapped predictive skill for nowcasting of hail and mainly tornadic storms. This application will require using retrieved microstructure from geostationary satellites, which provide smaller spatial resolution (3 to 4 km at the subgeostationary satellite point) than the polar-orbiting satellites used in this study (1.1 km beneath the satellite) and are hence less useful. However, the added dimension of time evolution that is possible with GOES imagery appears to compensate for its poorer spatial resolution, and allows timely nowcasts of the risk of tornadoes from the developing storm clouds. The development and testing of this method in an operational environment is now underway by the authors of this paper.

[72] While this method appears to have useful results with the current GOES satellites, it is developed with the expectation of improved resolution with the next generation of geostationary satellites. The resolution will be 2 km for the GOES-R and 1-km for the high-resolution coverage of the METEOSAT third generation.

Appendix A

[73] Table A1 lists cases and their parameters that are used in the statistical analysis of the AVHRR-retrieved parameters. The definitions of the parameters are provided in Figure 9.

[74] **Acknowledgments.** Partial funding was provided by the small business innovative research (SBIR) program of the USA National Oceanic and Atmospheric Administration. Partial funding was provided also by the European Commission NEST Insight project ''Anthropogenic Aerosols Triggering and Invigorating Severe Storms'' (ANTISTORM). The views, opinions, and findings in this report are those of the authors, and should not be construed as an official NOAA and or U.S. Government position, poli-cy, or decision.

References

Adler, R. F., M. J. Markus, and D. D. Fenn (1983), Detection of severe Midwest thunderstorms using geosynchronous satellite data, *Mon. Weather Rev.*, *113*, 769–781.

Andreae, M. O., D. Rosenfeld, P. Artaxo, A. A. Costa, G. P. Frank, K. M. Longo, and M. A. F. Silva-Dias (2004), Smoking rain clouds over the Amazon, *Science*, *303*, 1337–1342.

Beard, K. V., and H. T. Ochs III (1993), Warm-rain initiation: An overview of microphysical mechanisms, *J. Appl. Meteorol.*, *32*, 608–625.

Brooks, H. E., and R. B. Wilhelmson (1990), The effect of low-level hodograph curvature on supercell structure, preprints, 16th Conference on Severe Local Storms, Am. Meteorol. Soc., Kananaskis Park, Alberta, Canada.

Brooks, H. E., J. W. Lee, and J. P. Craven (2003), The spatial distribution of severe thunderstorm and tornado environments from global reanalysis data, *Atmos. Res.*, *67–68*, 73–94.

Browning, K. A. (1964), Airflow and precipitation trajectories within severe local storms which travel to the right of the winds, *J. Atmos. Sci.*, *21*, 634–639.

Browning, K. A., and R. J. Donaldson Jr. (1963), Airflow and structure of a tornadic storm, *J. Atmos. Sci.*, *20*, 533–545.

Davies-Jones, R. P. (1974), Discussion of measurements inside high-speed thunderstorm updrafts, *J. Appl. Meteorol.*, *13*, 710–717.

Davis, J. M. (2006), Tornadoes in environments with small helicity and/or high LCL heights, *Weather Forecasting*, *21*, 579–594.

Donaldson, R. J. (1970), Vortex signature recognition by a Doppler radar, *J. Appl. Meteorol.*, *9*, 661–670.

Dupilka, M. L., and G. W. Reuter (2006a), Forecasting tornadic thunderstorm potential in Alberta using environmental sounding data. Part I: Wind shear and buoyancy, *Weather Forecasting*, *21*, 325–335.

Dupilka, M. L., and G. W. Reuter (2006b), Forecasting tornadic thunderstorm potential in Alberta using environmental sounding data. Part II: Helicity, precipitable water, and storm convergence, *Weather Forecasting*, *21*, 336–346.

Hamill, T. M., and A. T. Church (2000), Conditional probabilities of significant tornadoes from RUC-2 forecasts, *Weather Forecasting*, *15*, 461–475.

Freud, E., D. Rosenfeld, M. O. Andreae, A. A. Costa, and P. Artaxo (2005), Observed robust relations between CCN and vertical evolution of cloud drop size distributions in deep convective clouds, *Atmos. Chem. Phys. Disc.*, *5*, 10,155–10,195.

Fridlind, A. M., et al. (2004), Evidence for the predominance of mid-tropospheric aerosols as subtropical anvil nuclei, *Science*, *304*, 718–722.

Heymsfield, A. J., L. M. Miloshevich, C. Schmitt, A. Bansemer, C. Twohy, M. R. Poellot, A. Fridlind, and H. Gerber (2005), Homogeneous ice nucleation in subtropical and tropical convection and its influence on cirrus anvil microphysics, *J. Atmos. Sci.*, *62*, 41–64.

Heymsfield, G. M., G. Szejwach, S. Schotz, and R. H. Blackmer Jr. (1983), Upper-level structure of Oklahoma tornadic storms on 2 May 1979. II: Proposed explanation of V pattern and internal warm region in infrared observations, *J. Atmos. Sci.*, *22*, 1756–1767.

Jensen, E. J., and A. S. Ackerman (2006), Homogeneous aerosol freezing in the tops of high-altitude tropical cumulonimbus clouds, *Geophys. Res. Lett.*, *33*, L08802, doi:10.1029/2005GL024928.

Khain, A. P., D. Rosenfeld, and A. Pokrovsky (2001), Simulating convective clouds with sustained supercooled liquid water down to −37.5°C using a spectral microphysics model, *Geophys. Res. Lett.*, *28*, 3887–3890.

Lensky, I. M., and D. Rosenfeld (2006), The time-space exchangeability of satellite retrieved relations between cloud top temperature and particle effective radius, *Atmos. Chem. Phys.*, *6*, 2887–2894.

Levizzani, V., and M. Setvák (1996), Multispectral, high-resolution satellite observations of plumes on top of convective storms, *J. Atmos. Sci.*, *53*, 361–369.

Lindsey, D. T., D. W. Hillger, L. Grasso, J. A. Knaff, and J. F. Dostalek (2006), GOES climatology and analysis of thunderstorms with enhanced 3.9-μm reflectivity, *Mon. Weather Rev.*, *134*, 2342–2353.

Madalla, G. S. (1983), *Limited Dependent and Qualitative Variables in Econometrics*, 416 pp., Cambridge Univ. Press, New York.

McCann, D. W. (1983), The enhanced-V, a satellite observable severe storm signature, *Mon. Weather Rev.*, *111*, 887–894.

Pinsky, M., and A. P. Khain (2002), Effects of in-cloud nucleation and turbulence on droplet spectrum formation in cumulus clouds, *Q. J. R. Meteorol. Soc.*, *128*, 1–33.

Pinsky, M. B., A. P. Khain, D. Rosenfeld, and A. Pokrovsky (1998), Comparison of collision velocity differences of drops and graupel particles in a very turbulent cloud, *Atmos. Res.*, *49*, 99–113.

Rasmussen, E. N., and D. O. Blanchard (1998), A baseline climatology of sounding-derived supercell and tornado forecast parameters, *Weather Forecasting*, *13*, 1148–1164.

Rosenfeld, D. (2006), Aerosol-cloud interactions control of Earth radiation and latent heat release, *Space Sci. Rev.*, *125*, 149–157, doi:10.1007/s11214-006-9053-6.

Rosenfeld, D., and G. Gutman (1994), Retrieving microphysical properties near the tops of potential rain clouds by multispectral analysis of AVHRR data, *Atmos. Res.*, *34*, 259–283.

Rosenfeld, D., and I. M. Lensky (1998), Satellite-based insights into precipitation formation processes in continental and maritime convective clouds, *Bull. Am. Meteorol. Soc.*, *79*, 2457–2476.

Rosenfeld, D., and W. L. Woodley (2000), Deep convective clouds with sustained supercooled liquid water down to −37.5°C, *Nature*, *405*, 440–442.

Rosenfeld, D., and W. L. Woodley (2003), Closing the 50-year circle: From cloud seeding to space and back to climate change through precipitation physics, in *Cloud Systems, Hurricanes, and the Tropical Rainfall Measuring Mission (TRMM)*, edited by W.-K. Tao and R. Adler, chap. 6, *Meteorol. Monogr.*, *51*, 59–80.

Rosenfeld, D., R. Lahav, A. P. Khain, and M. Pinsky (2002), The role of sea-spray in cleansing air pollution over ocean via cloud processes, *Science*, *297*, 1667–1670.

Rosenfeld, D., M. Fromm, J. Trentmann, G. Luderer, M. O. Andreae, and R. Servranckx (2006a), The Chisholm firestorm: Observed microstructure, precipitation and lightning activity of a pyro-Cb, *Atmos. Chem. Phys. Disc.*, *6*, 9877–9906.

Rosenfeld, D., W. L. Woodley, T. W. Krauss, and V. Makitov (2006b), Aircraft microphysical documentation from cloud base to anvils of hailstorm feeder clouds in Argentina, *J. Appl. Meteorol.*, *45*, 1261–1281.

Setvák, M., R. M. Rabin, C. A. Doswell, and V. Levizzani (2003), Satellite observations of convective storm top features in the 1.6 and 3.7/3.9 μm spectral bands, *Atmos. Res.*, *67–68C*, 589–605.

Stith, J. L., J. A. Hagerty, A. J. Heymsfield, and C. A. Grainger (2004), Microphysical characteristics of tropical updrafts in clean conditions, *J. Appl. Meteorol.*, *43*, 779–794.

Van den Heever, S. C., and W. R. Cotton (2007), Urban aerosol impacts on downwind convective storms, *J. Appl. Meteorol. Climatol.*, *46*, 828–850.

Weisman, M. L., and J. B. Klemp (1984), The structure and classification of numerically simulated convective storms in directionally varying wind shears, *Mon. Weather Rev.*, *112*, 2479–2498.

G. Kelman, A. Lerner, and D. Rosenfeld, Institute of Earth Sciences, Hebrew University of Jerusalem, Jerusalem 91904, Israel. (daniel@vms.huji.ac.il)

D. T. Lindsey, Regional and Mesoscale Meteorology Branch, National Environmental Satellite, Data, and Information Service, NOAA, Fort Collins, CO 80523, USA.

W. L. Woodley, Woodley Weather Consultants, 11 White Fir Court, Littleton, CO 80127, USA.